GSI

GSI-Preprint-99-30
August 1999

RELATIVISTIC RADIOACTIVE BEAMS: A NEW ACCESS TO NUCLEAR-FISSION STUDIES

K.-H.Schmidt, S. Steinhäuser, C. Böckstiegel, A. Grewe, A. Heinz, A.R. Junghans, J. Benlliure, H.-G. Clerc, M. de Jong, J. Müller, M. Pfützner, B. Voss

(accepted for publication in Nucl. Phys. A)

Gesellschaft für Schwerionenforschung mbH
Planckstraße 1 • D-64291 Darmstadt • Germany
Postfach 11 05 52 • D-64220 Darmstadt • Germany

Relativistic Radioactive Beams:

A New Access to Nuclear-Fission Studies*

K.-H. Schmidt[1], S. Steinhäuser[2], C. Böckstiegel[2], A. Grewe[2], A. Heinz[2], A. R. Junghans[1], J. Benlliure[3], H.-G. Clerc[2], M. de Jong[2], J. Müller[2], M. Pfützner[4], B. Voss[1]

[1] *Gesellschaft für Schwerionenforschung, Planckstraße 1, D-64291 Darmstadt, Germany*

[2] *Institut für Kernphysik, Technische Universität Darmstadt, Schloßgartenstraße 9, D-64289 Darmstadt, Germany*

[3] *Facultad de Fisica Universidad de Santiago de Compostela E-15706 Santiago de Compostela, Spain*

[4] *Instytut Fizyki Doswiadczalnej, Uniwersytet Warszawski, ul Hoza 69, 00-381 Warszawa, Poland*

Key words: Nuclear reaction, radioactive beams, nuclear fission, measured fission-fragment elemental yields for ^{205,206}At, $^{204\text{-}209}$Rn, $^{206\text{-}212,217,218}$Fr, $^{209\text{-}219}$Ra, $^{212\text{-}226}$Ac, $^{217\text{-}229}$Th, $^{224\text{-}232}$Pa, $^{230\text{-}234}$U and total kinetic energies for $^{210\text{-}215,217\text{-}219}$Ra, $^{215\text{-}223}$Ac, $^{221\text{-}229}$Th, $^{226\text{-}232}$Pa, $^{232\text{-}234}$U, transition from symmetric to asymmetric fission, deduced even-odd effect

PACS: 24., 24.30.Cz, 24.75.+I, 25.20.-x, 25.60.-t, 25.70.Mn, 25.85.-w, 25.85.Jg, 27.80.+w, 27.90.+b, 29.30.Aj, 29.40.-n, 29.40.Mc

Abstract: The secondary-beam facility of GSI Darmstadt was used to study the fission properties of 70 short-lived radioactive nuclei. Most of them have not been accessible so far in conventional fission experiments. Relativistic secondary projectiles were produced by fragmentation of a 1 *A* GeV ^{238}U primary beam and identified in nuclear charge and mass number. Using these reaction products as secondary beams, the giant resonances, mostly the giant dipole resonance, were excited by electromagnetic interactions in a secondary lead target, and fission from excitation energies around 11 MeV was induced. The fission fragments were identified in nuclear charge, and their velocity vectors were determined. Elemental yields and total kinetic energies have been obtained for a number of neutron-deficient actinides and pre-actinides. The characteristics of multimodal fission of nuclei around ^{227}Th were systematically investigated. The proton even-odd effect was determined for all systems.

* This work forms part of the PhD theses of C. Böckstiegel, A. Grewe, A. Heinz, and S. Steinhäuser.

1. INTRODUCTION

Nuclear fission provides unique information on the reordering of nucleons in a large-scale collective motion. The signatures of shell structure and pairing correlations show up in fission from excitation energies below or slightly above the fission barrier. Data on low-energy nuclear fission have general implications on the understanding of the influence of shell structure on nuclear dynamics and of the viscosity of cold nuclear matter. However, in spite of several decades of intense work, the experimental information on nuclear fission has been still rather limited. In particular, the choice of fissioning systems to be investigated has been very much restricted by technical constraints. Therefore, an effort has been made recently [1] to overcome the severe restrictions of conventional fission experiments in order to extend the body of experimental data. The present work reports on an experiment performed with a novel technique: The fission of relativistic secondary projectiles was studied in flight. The benefit of the inverse kinematics on the electromagnetic excitation mechanism [2] and on the detection of the fission fragments [3,4,5,6,7] has been demonstrated in several experiments with relativistic ^{238}U primary projectiles. In order to extend the investigations to many other fissioning nuclei, the present work takes advantage of the relativistic radioactive beams available at GSI. Since this experiment is representative for the potential progress in nuclear physics brought about by the use of secondary beams, the specific experimental conditions which differ considerably from those of conventional fission studies are described in detail. In addition, the large body of new data is presented, and a first analysis of the results is given. However, first the present understanding of structural effects in fission will be shortly summarised in order to work out the open problems where progress is most urgently needed.

1.1 Shell structure

Different components appear in the yields and in the kinetic-energy distributions of the fission fragments from different compound nuclei. This is illustrated in Figure 1, where some examples of previously measured mass distributions of fission fragments are shown on a chart of the nuclides. The relation of the observed structures to shell effects of the fissioning system was pointed out [8,9,10,11]. It has been proposed to understand these findings as a superposition of different components, named "fission modes" or "fission channels" [12,13,14,15]. At low excitation energies, all nuclei with mass numbers from 230 to about 256 predominantly divide into a heavier and a lighter fragment while symmetric splits are strongly suppressed. Over this whole range, the gross behaviour of the fission process is governed by the constant position of the heavy component around mass number 138 (ref. [16]). The fission characteristics of these nuclei can rather well be described by a superposition of three fission channels: two mass-asymmetric channels ("standard I" and "standard II") as well as a weak contribution of the "superlong" channel at mass symmetry. When considering the deformation of the nascent fragments in the scission configuration, Standard I is characterised by a spherical heavy fragment around mass number 134 and a deformed light fragment. Standard II is characterised by a deformed heavy fragment near mass number 145 and a slightly deformed or spherical light fragment. Finally, in the "superlong" channel both fragments are strongly deformed. The latter becomes more important in fission at higher excitation energies. Some data are available that reveal remarkably different features in the mass distributions of fissioning nuclei with masses larger than 256 and of nuclei with masses lower than 230, respectively. First, for a very limited number of nuclei around ^{258}Fm, a very specific symmetric channel shows up with

a narrow mass distribution and exceptionally high kinetic energies (refs. [17,18,19,20]) which can be understood as the formation of two spherical fission fragments near the doubly magic ^{132}Sn (refs. [14,21,22,23,24]). Secondly, for a few nuclei around ^{227}Ac, triple-humped mass distributions have been measured (refs. [25,26,27,28,29,30,31,32]), and, finally, near ^{213}Ac symmetric fission prevails (ref. [27,33]).

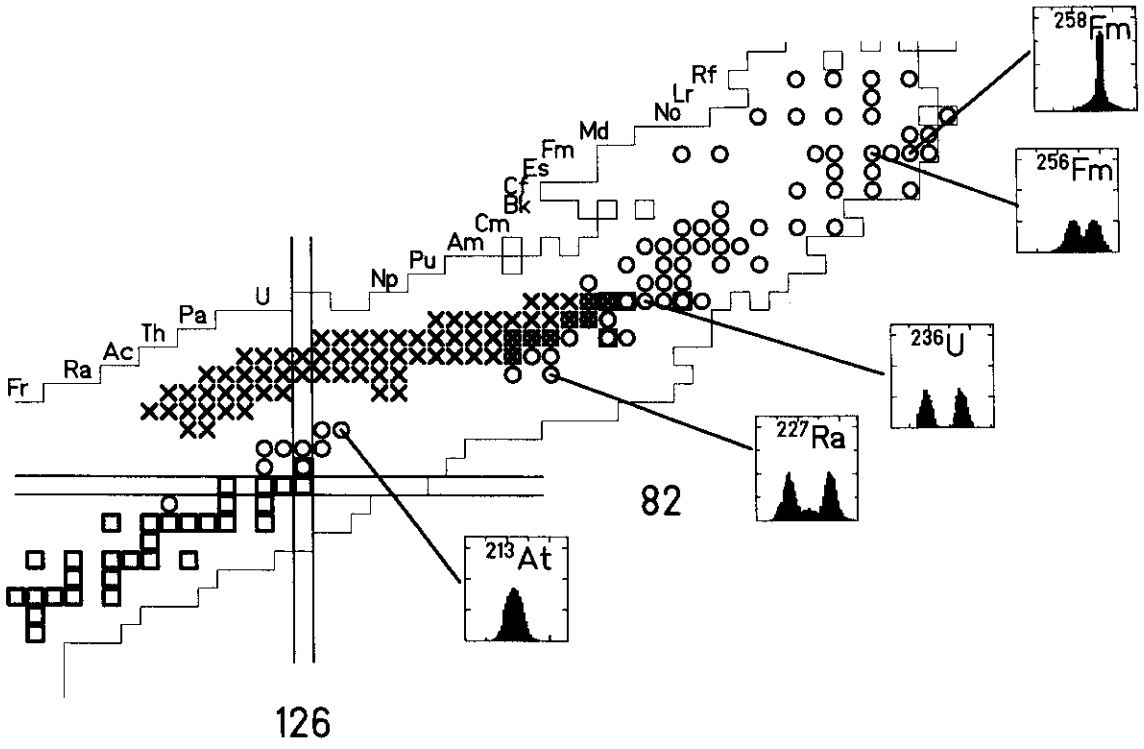

Figure 1: Isotopes investigated in low-energy fission. Circles: Mass distributions measured in previous experiments for excitation energies less than 10 MeV above the fission barrier. Crosses: Systems investigated in the present experiment. Additionally, examples of previously measured fission-fragment mass distributions are shown (data from refs. [20,30,38,52]). For orientation, the primordial isotopes are indicated by squares.

According to refs. [13,14,15], the fission channels are identified with valleys in the potential-energy surface of the highly deformed system due to shell effects. The valleys extend in the direction of elongation, and they reach from deformations near the fission barrier to scission. However, it is not clear, how the fissioning system evolves on the way from saddle to scission. There exist models in which the characteristics of the fission fragments were exclusively deduced from the properties of the scission configuration, for example the early statistical fission model of Fong [8] or the rather successful thermodynamical model of Wilkins, Steinberg and Chasman [11]. Others expect a decisive influence of the density of transitional states at the fission barrier on the fission process [34,35,36,37,38,39,40]. A realistic description would have to consider the complex nature of the shell structure with possible bifurcations of different fission valleys (see for example ref. [14]) as well as the influence of viscosity and inertia on the collective motion from saddle to scission. The description of fission dynamics has been a challenge for a long time, see for example refs. [41,34,42,43]. Most prom-

ising attempts are actually being made [44,45], but a complete dynamical description of low-energy fission is not yet available.

1.2 Pairing correlations

As one of the most outstanding features of fission-fragment yields in low-energy fission of compound nuclei with even number of protons, the production of fission fragments with even number of protons has been found to be generally enhanced [46]. This was interpreted as a signature that completely paired proton configurations are preserved up to the scission point [47] with a high probability. It was assumed that the even-odd structure would disappear when at least one proton pair was broken due to the heating of the fissioning system. On the basis of this assumption, conclusions were drawn from the observed even-odd effect on the heating of the nucleus undergoing fission on the way to the scission point, and hence about the viscosity of cold nuclear matter [48].

While the number of neutrons of the fission fragments is strongly influenced by neutron evaporation after fission, the number of protons carries direct information on scission. However, identification methods faster than the beta half-lives have to be used. This criterion is met for example by experiments at LOHENGRIN [49,50,51,52,53,54,55] and COSI FAN TUTTE [56,57,58] at the neutron high-flux reactor of the Institute Laue-Langevin in Grenoble (France). Also the identification method used in the present work is faster than beta decay by many orders of magnitude.

Previously measured data indicate that the even-odd effect in elemental yields varies strongly from one fissioning system to another. In addition, for some of the systems, a variation of the even-odd structure as a function of the charge split has been found [59,60]. These variations have been interpreted as a corresponding variation of the energy that is dissipated between saddle and scission [47]. In particular, it was concluded that, comparing different fissioning nuclei, the amount of dissipated energy grows strongly with increasing fissility and that, comparing different charge splits of the same system, extremely asymmetric fission processes proceed with especially low dissipation [59,60].

1.3 Experimental situation

The experimental knowledge on nuclear fission is still rather limited. Up to now, low-energy fission, that means fission from excitation energies below or close to the fission barrier, could only be investigated for spontaneously fissioning nuclei and for those nuclei that could be reached by exciting sufficiently long-lived target nuclei. During almost six decades since the discovery of nuclear fission, experimental studies on low-energy fission were restricted to about 80 fissioning nuclei (see Figure 1). They represent only about 15 percent of all known nuclei with Z above 82. Previous attempts to overcome these restrictions were limited to a few very specific cases (e.g. ref. [61]) or they could not reach sufficiently low excitation energies [32,62]. Data on the fission properties of nuclei far from the beta-stability line or in the region between ^{213}At and ^{225}Ra are urgently needed in order to substantially improve the experimental data basis for the understanding of the influence of nuclear structure on fission dynamics. The transitional region below ^{236}U from asymmetric to symmetric fission is particularly interesting, because here the competition between different fission channels is ex-

pected to reflect structural effects in the potential-energy landscape in a very sensitive way, similar to the transitional region around ^{257}Fm.

The data basis for the even-odd structure in fission-fragment yields is even much more restricted. Therefore, general conclusions on pair breaking in fission must be considered with precaution. It would be highly desirable to extend the experimental knowledge on fission-fragment nuclear-charge distributions in a systematic way.

In the present work we present the details of the novel experimental technique, the data analysis and the general results on the influence of shell effects and pairing correlations on fission-fragment nuclear-charge distributions and total kinetic energies for neutron-deficient actinides and preactinides.

2. THE EXPERIMENTAL METHOD

2.1 The benefit of radioactive beams

During the last years, secondary beams became available in many laboratories. Numerous experiments with short-lived radioactive projectile nuclei have initiated important progress in the understanding of nuclear structure, in particular for exotic nuclei far from the beta-stability line. While most of the activities concentrated on rather light nuclei -- ^{11}Li is a famous example -- the present work reports on a first series of experiments performed with beams of heavy, short-lived radioactive nuclei in order to extend our knowledge on nuclear fission.

The use of radioactive beams gives access to a large new field of fissioning systems and thus overcomes a severe restriction of conventional experimental techniques. The secondary-beam facility of GSI Darmstadt offers unique possibilities to provide secondary beams of neutron-deficient actinides and preactinides, produced by fragmentation of ^{238}U. Within the limits given by the primary-beam intensity and the fragmentation cross sections [63,64], nuclear-charge and mass number of the nuclei to be investigated can freely be selected by tuning the fragment separator. Excitation in-flight of the relativistic secondary projectiles in the strong electromagnetic field of high-Z target nuclei was used to populate states in the vicinity of the fission barrier with the high cross sections of several barns required for experiments with low-intensity secondary beams. With a probability which depends on the actual nucleus considered, the electromagnetic excitation leads to fission. The fission fragments were recorded with a dedicated detector set-up to determine their yields and kinetic energies [1,65], as well as the fission cross sections [66]. Since the fission in inverse kinematics provided the fission products with very high velocities in the laboratory frame, they were fully stripped. Therefore, the elemental fission-fragment yields could be determined with high resolution. This allowed also to increase our knowledge on even-odd structure in fission considerably.

2.2 Preparation of the secondary beams

The secondary beams were produced by fragmentation of a ^{238}U primary beam at 1 *A* GeV in a 657 mg/cm^2 Be target at the entrance of the fragment separator FRS [67]. The fragment separator with the most important detectors used to prepare the secondary beams is schematically shown in Figure 3. The separator was operated as a momentum-loss achromat [68]. A

profiled aluminium layer and the scintillation detector in the intermediate image plane of the separator acted together as a thick energy degrader. Niobium foils were used to maximise the fraction of totally stripped ions both behind the production target and behind the intermediate energy degrader in order to improve the ion-optical separation. The secondary projectiles were separated by recording their horizontal positions at the intermediate image plane and at the exit by means of position-sensitive scintillation detectors [69]. Both detectors were read out by photomultipliers HAMAMATSU R2083, equipped with bases which allow for high counting rates up to 10^5 per second without deteriorating the time resolution in the order of 100 ps (FWHM).

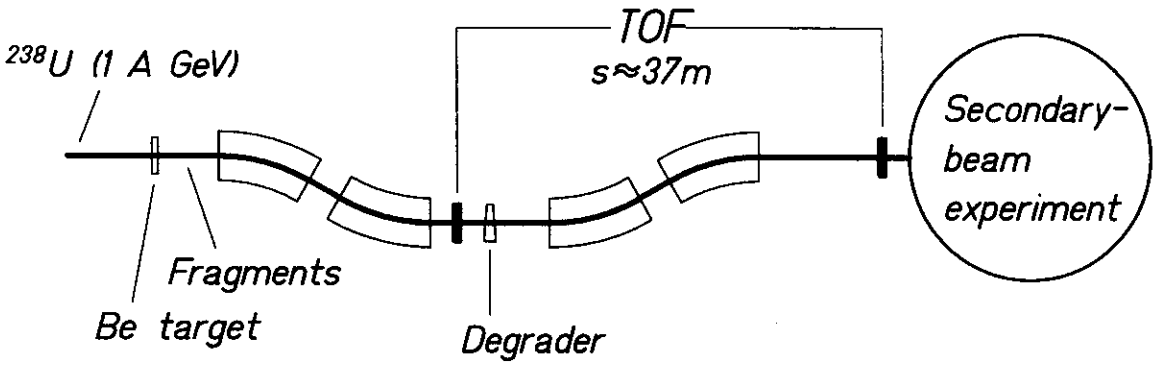

Figure 2: Schematic drawing of the fragment separator used to prepare the secondary beams. Only the production target, the four dipole magnets, the energy degrader and the detectors used to identify the fragmentation products are indicated. The set-up for the secondary-beam experiment is shown in Figure 4.

The two-dimensional identification spectrum for the setting on ^{229}Pa is shown in Figure 3 (left part). The vertically separated bands correspond to different elements. While the nuclear charge is now sufficiently well determined, the different isotopes still partly overlap due to their velocity distribution. Therefore, the nuclear mass is calculated from the magnetic rigidity and the time-of-flight, recorded in the second section of the separator by the scintillation detectors. The mass resolution achieved $(A / \Delta A = 410)$ for the series of protactinium isotopes is demonstrated in Figure 3 (right part). In both spectra, ions that are not fully stripped in either section of the separator have already been suppressed strongly as outlined in refs. [63,70,71], where one can also find a full description of the identification method. In ref. [71] the production cross sections that determine the secondary-beam intensities are given, too. (The reaction ^{238}U (950 *A* MeV) + Cu, investigated in ref. [71], provides rather similar isotopic cross sections as the reaction ^{238}U (1 *A* GeV) + Be, used in the present work.) With an average primary-beam intensity of 10^7 per second, secondary-beam intensities of 100 per second for a specific isotope could be obtained in favourable cases. Due to their relativistic velocities, the secondary projectiles pass the separator in about 300 ns. Therefore, also very short-lived nuclei like the 128-neutron isotones can be investigated. We want to stress that the separation in-flight is insensitive to the chemical properties of the secondary projectiles.

A list of the most important layers of matter in the experimental set-up that the secondary projectiles and the fission fragments, respectively, had to traverse, is given in Table 1. This list reveals that the rate of secondary reactions along the beam line is not negligible. There-

fore, the data analysis has to provide the appropriate tools to extract the relevant experimental information and to correct for background contributions. In the following, we will describe how the fission events originating from electromagnetic interactions with the lead nuclei in the secondary target are distinguished from fission after nuclear interaction in the lead target and the large amount of parasitic reactions in other layers of matter in the beamline. Moreover, the energy loss in the different layers of matter along the beamline before and after fission consumes most of the initial energy of the secondary beam. As we will see later, this makes it a difficult task to determine the kinetic energy that is released in the fission process.

Table 1: Layers of matter in the beamline.

Material	thickness mg/cm^2	Position mm	E/A MeV	relative nuclear reaction rate	Purpose
		target area of the FRS:			
Beryllium	657.0	-2270	951 (b)	0.14 (d)	Production target
Niobium	212.0	-2268	938 (b)	0.008 (e)	Stripper foil
		midplane of the FRS:			
Plastic	516	-934	896 (b)	0.135 (e)	ToF detector
Aluminium	3878 (a)	0	605 (b)	0.312 (e)	Energy degrader
Niobium	108.4	62.5	598 (b)	0.004 (e)	Stripper foil
		Exit of the FRS:			
Titanium	90.2	930	591 (b)	0.006 (e)	Vacuum window
Air	170.0		576 (b)	0.026 (e)	
Plastic	543.0	2323	531 (b)	0.145 (e)	ToF detector, light shield
Air	39.0		527 (b)	0.039 (e)	
Lead	3030.0	2619	---	0.067 (e)	Secondary target
P10	66.5	2619	369 (c)	0.005 (e)	Counting gas of active target
Air	165.0		355 (c)	0.018 (f)	
Plastic	335.0	4676	337 (c)	0.061 (f)	Fission trigger, light shield
Air	54.0		335 (c)	0.006 (f)	
P10	171.0	5019	327 (c)	0.009 (f)	Twin MUSIC
Air	227.0		306 (c)	0.025 (f)	
Plastic	543.0	7950	273 (c)	0.099 (f)	ToF wall, light shield (front)
Plastic	543.0	8030	238 (c)	0.099 (f)	ToF wall, light shield (back)

The positions are given relative to the entrance plane of the first quadrupole in the target area, relative to the central image plane near the midplane, and relative to the endplane of the last quadrupole at the exit of the separator.
The plastic layers indicated consisted mainly of scintillator plates (BC420 from BICRON). Its main constituent is $(C_9H_{10})_n$.
(a) This is a typical value that was slightly varied during the experiment in order to obtain the same velocity in the centre of the secondary target for all secondary beams.
(b) Mean energy of ^{229}Pa behind the indicated layer when produced in the middle of the target.
(c) Mean energy of ^{114}Pd behind the indicated layer when produced in the middle of the secondary lead target by fission in a direction perpendicular to the beam.
(d) Reaction rate of ^{238}U in the indicated layer.
(e) Reaction rate of ^{229}Pa in the indicated layer.
(f) Reaction rate of ^{114}Pd in the indicated layer.
All reaction rates were calculated according to ref. [72]. The energy losses were calculated as described in ref. [68].

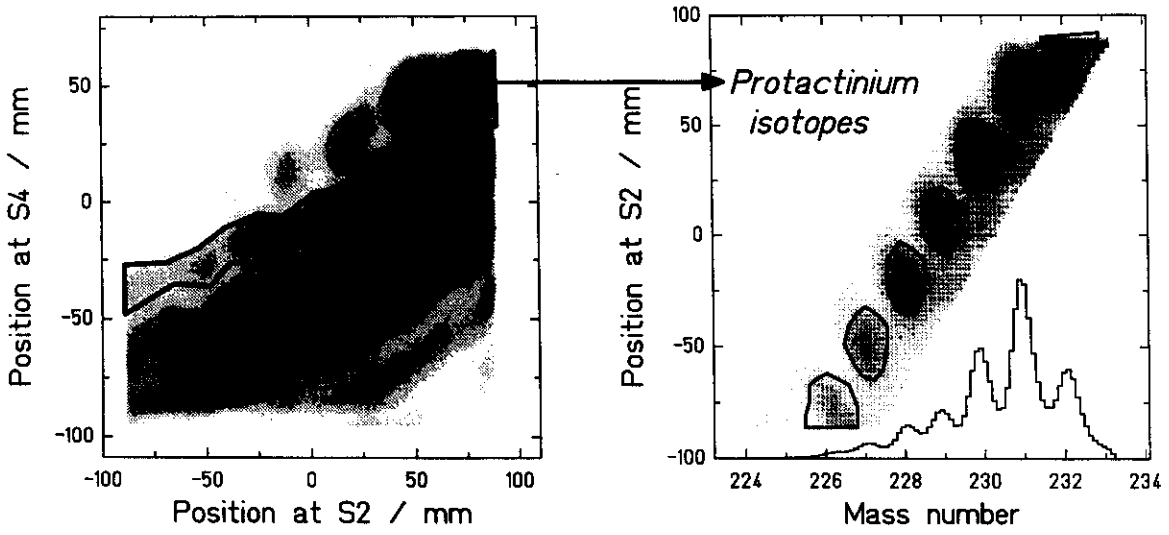

Figure 3: Isotopic identification of the secondary beams. Left part: Two-dimensional cluster plot of the horizontal positions of the secondary-beam particles in the intermediate image plane (S2) and at the exit (S4) of the fragment separator for one ion-optical setting that was centred on ^{229}Pa. A polygon window on protactinium isotopes is indicated. Right part: Two-dimensional cluster plot of mass number and the horizontal position at the intermediate image plane for protactinium isotopes. The projection on the mass axis is additionally given.

2.3 The set-up for the secondary-beam experiment

The experimental set-up used for the secondary-beam fission studies is schematically shown in Figure 4. It consisted of a scintillation detector, an active secondary target, a subdivided double scintillator, a twin multiple-sampling ionisation chamber (twin MUSIC), and a time-of-flight wall. The first scintillation detector had several tasks. First, it supplied the horizontal position and the stop signal for the time-of-flight of the secondary projectiles at the exit of the fragment separator for the ion-optical analysis shown in Figure 3. In addition, it acted as a secondary target with predominantly nuclear interactions and a negligible amount of electromagnetic excitations. Finally, it served as a start detector for determining the velocities of the fission fragments. The active target contained the lead target material, providing a probability for electromagnetic excitations of a few percent. The target foils were mounted inside a subdivided ionisation chamber filled with P10 counting gas. A positive voltage of +1000 V was supplied to the first, the third and the fifth lead foil, and the charge signals of these anodes due to ionisation of the counting gas were recorded. Figure 5 shows the operation principle of the active target, and Figure 6 demonstrates how the signals allowed to determine the layer in which fission was induced. The key information for this purpose is the reduction of the energy loss by roughly a factor of two when fission takes place. When the pulse height of the third anode is analysed in addition, the lead foil in which the secondary projectile fissions can unambiguously be determined. In this way, any events from fission reactions in the other layers of matter in the beamline (see Table 1) are suppressed.

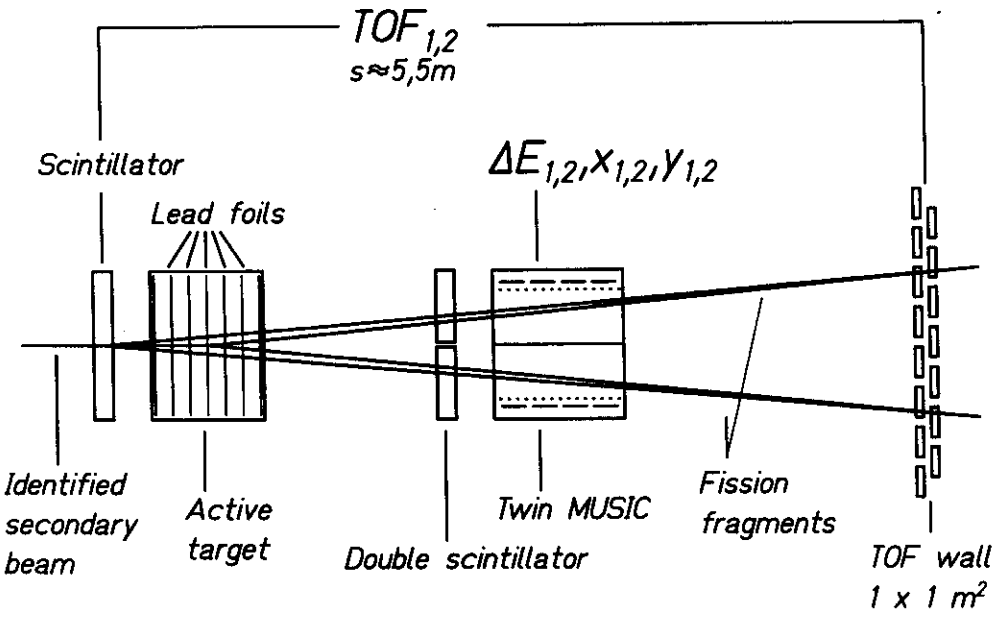

Figure 4: Schematical drawing of the set-up for the fission experiment with secondary beams.

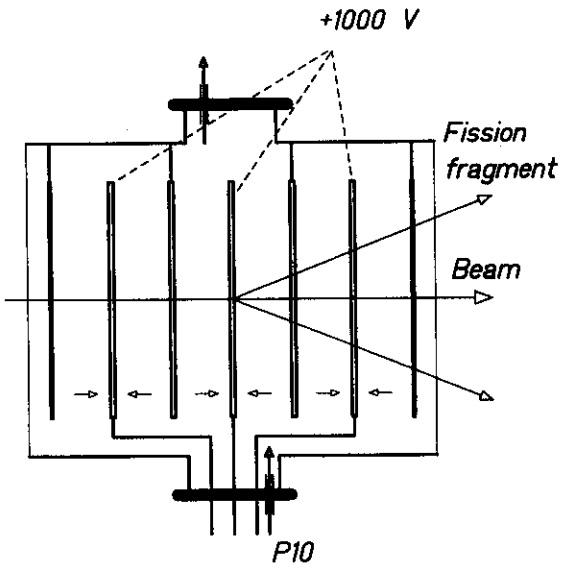

Figure 5: Schematic drawing of the active target and its operation principle. The target is equipped with 5 lead foils (≈600 mg/cm² each). Thin aluminium foils (27 mg/cm² each) form the first and the last cathode. The small arrows indicate the drift direction of the electrons. The charge signals of the anodes (1st, 3rd and 5th lead foil) are recorded.

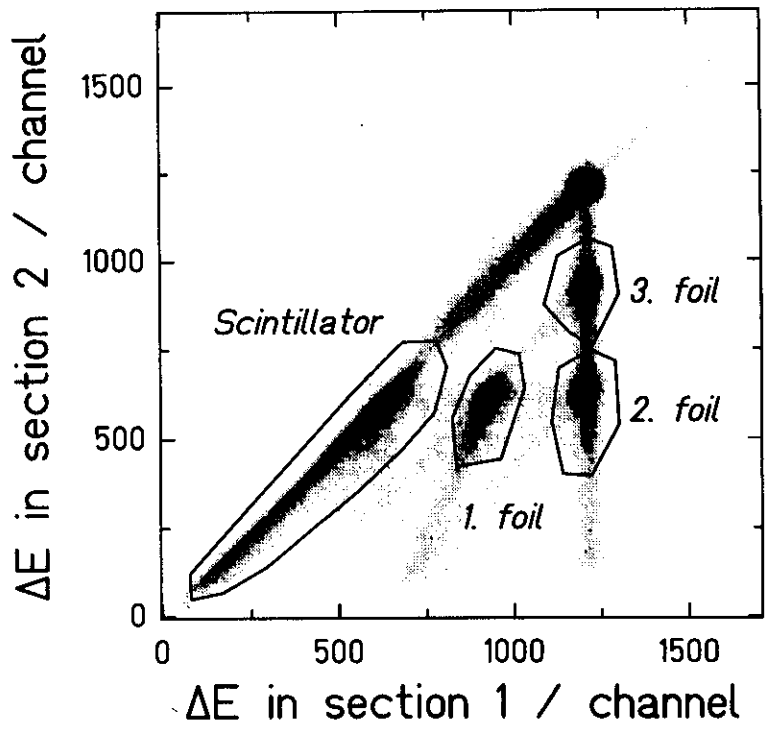

Figure 6: Cluster plot of the pulse heights of the first and second anode signals of the active target. Fission products from the different layers appear as well separated peaks on top of long lines originating from fragmentation. The layer in which fission was induced can easily be determined by the indicated polygon windows. Fission in the first, the second and the third lead foil can be distinguished from fission in the layers in front of the first lead foil (mostly induced in the scintillator plate in front of the active target).

The second, subdivided scintillation counter with a thickness of 3 mm, mounted in front of the twin MUSIC, served as a fast trigger. A coincidence of signals in both sections was required in order to register fission events only. This fast trigger reduced the load of the data acquisition by almost an order of magnitude. The twin MUSIC recorded the energy-loss signals of both fission fragments in the P10 counting gas separately. The dimensions of the total active volume were 600 mm in length, 400 mm in height, and 600 mm in width. The common cathode was mounted horizontally at the level of the beam axis. Thus, the high concentration of positive ions from the intense non-fissioning secondary projectiles could not interfere with the electrons liberated by the fission fragments in the counting gas. In this way, losses due to recombination were avoided. In addition, the twin MUSIC supplied the information on the horizontal and the vertical positions of the fission fragments by means of the pulse-height ratio of the diagonally subdivided anodes and by means of the drift time of the electrons, respectively. The position resolution was better than 6 mm in horizontal and better than 0.5 mm in vertical direction (FWHM).

The time-of-flight of the fission fragments was determined with a resolution of better than 170 ps (FWHM) by use of a large time-of-flight wall that was mounted 5.5 m downstream the start detector. The time-of-flight wall consisted of 15 horizontal stripes 1 m long, 100 mm

high, and 5 mm thick, mounted with an overlap of 33.3 mm in vertical direction. It covered a surface of 1 m^2. The scintillation material was BC420 from BICRON. One additional stripe was mounted vertically in order to facilitate the time calibration of the different stripes. The scintillation detectors where read out by 32 photomultipliers (type H2431sel) from HAMAMATSU.

The energy-loss signals of fission products recorded in the twin MUSIC and corrected for the slight position dependence are shown in Figure 7 as a function of the time-of-flight. Due to the thick secondary target and due to the large recoil induced in the fission process, the velocity distribution is very broad. However, the velocity being determined, the nuclear charges of all fission products could be measured with high resolution (see Figure 8).

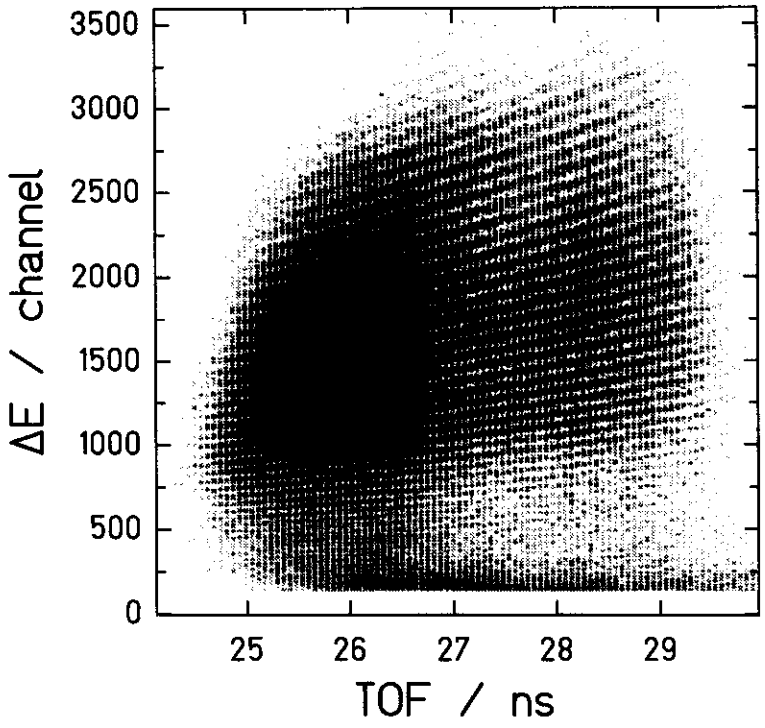

Figure 7: Two-dimensional cluster plot of the energy loss recorded in the twin MUSIC and the time-of-flight for fission fragments of a composite $^{223...229}$Th secondary beam.

Due to the high velocity of the secondary projectiles, the fission fragments were emitted in forward direction inside a cone with angles up to about 60 mrad with respect to the secondary-beam direction. The detectors were designed to cover all fission fragments produced in the first scintillation detector and in the active target for all secondary projectiles delivered by the fragment separator. However, with a probability of 10 % both fission fragments hit the same part of the second, subdivided scintillation detector used as fission trigger, and in these cases no trigger was generated. Considering additional losses due to the limited granularity of the time-of-flight wall and insufficient charge collection for tracks close to the cathode of the twin MUSIC, the detection efficiency amounted to 81 %.

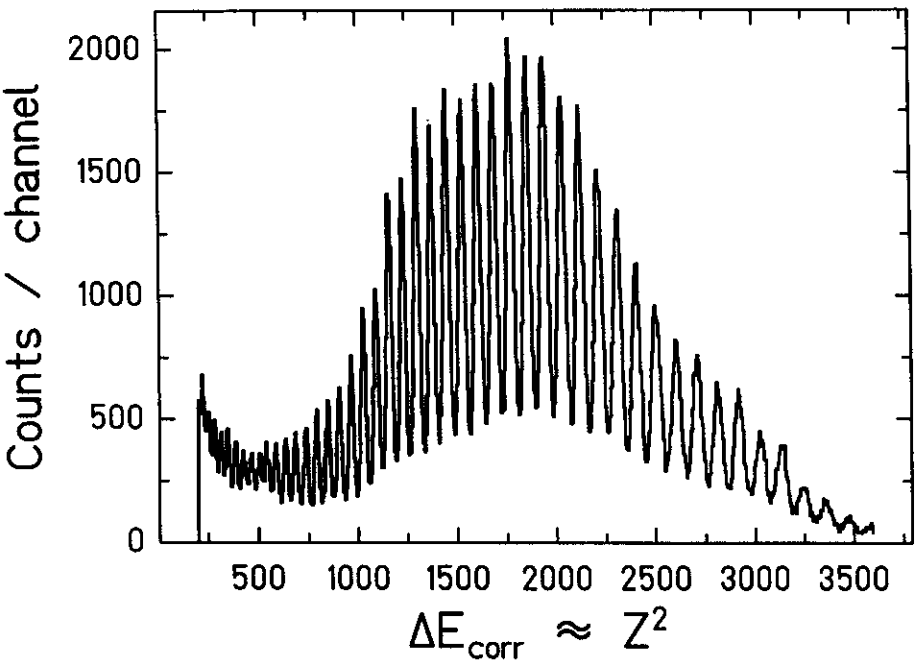

Figure 8: Energy-loss signal of the twin MUSIC, corrected for the velocity dependence, as obtained for the reaction products of a composite $^{223...229}$Th secondary beam from the secondary lead target. The scale of the energy loss corresponds approximately to the square of the nuclear charge.

2.4 Considerations of counting rates

The success of a secondary-beam experiment depends essentially on an efficient use of the limited beam intensity. Since two consecutive reactions are involved, this aspect is much more crucial here than in a primary-beam experiment. In the following we will consider the experimental conditions of the present fission experiment from this point of view.

We define the quantity L_{sec} as an appropriate figure of merit of the efficiency of the experiment:

$$L_{sec} = (N_{t1}/S)\ \varepsilon_1\ \sigma_1\ (N_{t2}/S)\ \sigma_2\ \varepsilon_2\ N_{sec} \qquad (1)$$

It corresponds to the ratio of detected secondary-reaction products to incoming primary projectiles. Table 2 lists the definitions and the values of the parameters of equation (1).

With the values given in Table 2, the figure of merit amounts to $L_{sec} = 3.2\times10^{-6}$. Owing to this remarkably high value, the rate of secondary reaction products attains $n_{sec} = n_p \times L_{sec} =$ 30/s which allowed to perform the present experiment even with the low primary-beam intensity of $n_p = 10^7$/s. Several conditions contribute to the efficient use of the beam. First, the magnitude of the cross sections involved is all-important. Another important parameter is the target thickness that is very large. Since two targets are involved, this parameter even enters twice. In addition, a high transport efficiency of the secondary beam and a high efficiency in detecting the reaction products that amount to almost 100% were reached in the present ex-

periment. Finally, due to its large acceptance, the fragment separator provided about 20 isotopes simultaneously in one setting, thus increasing the efficiency of the experiment accordingly.

Table 2: Characteristic parameters that define the counting rate of secondary reaction products in the present experiment. The cross section σ_2 includes only fission after electromagnetic excitation.

Parameter	Explanation	Typical value
N_p	Intensity of primary beam	10^7/s
N_{t1}/S	Atoms per area in primary target	4.4×10^{22}/cm^2
σ_1	Cross section of primary reaction	$\approx$1 mb = 10^{-27}cm^2
ε_1	Transport efficiency to secondary target	0.5
N_{t2}/S	Atoms per area in secondary target	8.8×10^{21}/cm^2
σ_2	Cross section of secondary reaction	$\approx$1 b = 10^{-24}cm^2
ε_1	Detection efficiency for secondary products	0.81
N_{sec}	Simultaneously measured secondary beams	$\approx$20

These considerations reveal that the secondary-beam intensity that is often regarded as the key parameter for the feasibility of a secondary-beam experiment is only one of several parameters that determine the counting statistics of the secondary reaction products. Another very important parameter for the present experiment is the high beam energy of 1 *A* GeV that enters indirectly on several places. First, it allows to use very thick targets for the secondary-beam production and for the secondary reaction to be studied. However, it also assures the high transport efficiency ε_1 of the secondary beam and, moreover, the simultaneous investigation of about 20 species without any loss of detection efficiency. It also facilitates to reach a high detection efficiency for the secondary-reaction products. The high beam energy is also mandatory for the ion-optical separation of the heavy secondary projectiles, avoiding ambiguities and losses due to broad ionic charge-state distributions that would occur at lower energies. As a last point, we would like to mention the strong energy dependence of the cross section for electromagnetic excitations.

We conclude that the experiment was successful only because experimental methods were applied which were well adapted to the specific conditions brought about by the secondary beams.

2.5 Extraction of elemental yields

In order to extract fission-fragment elemental yields after electromagnetic-induced fission, fission events originating from nuclear interactions with the lead target nuclei have to be suppressed. Most part of the nuclear-induced fission can be identified on an event-by-event basis. The procedure is similar to that described in ref. [73] which was used in a preceding experiment. However, since the experimental set-up has been modified, the resolution of the detectors was appreciably improved, and it was possible to use a more elaborate procedure.

Fundamentally different features are expected for fission after electromagnetic excitations and after nuclear interactions: While electromagnetic excitations preserve the number of protons in the secondary projectiles, nuclear interactions in most cases remove several protons prior to fission. Evaporation of protons prior to fission as well as after fission following electromagnetic excitations is very improbable and may be disregarded in most cases. Therefore, the good nuclear-charge resolution of the experiment (see Figure 8) allowed to reconstruct spectra of the nuclear charge of the fissioning nucleus by summing up the nuclear-charges of the two fission fragments. The measured charge-sum spectra of the fission fragments produced in the scintillator target and in the lead target from a ^{226}Th secondary beam are shown in Figure 9 (upper part). As expected, the charge-sum spectrum of fission events from the lead target is strongly enhanced for $Z_{cn} = 90$ if compared to the spectrum of fission events from the scintillator. This enhancement can be attributed to fission after electromagnetic excitations in the lead target. Electromagnetic excitations in the scintillation material (C_9H_{10}) are negligible.

Fission events that are induced by electromagnetic excitations in the lead target can be highly enriched in the data analysis on an event-by-event basis by imposing a condition on the $Z_{cn} = 90$ peak in the charge-sum spectrum (Figure 9, upper part). The nuclear-charge spectrum of fission fragments, accumulated under this condition, is shown in the middle part of Figure 9. However, this spectrum still contains a number of fission events induced by nuclear interactions in which only neutrons are removed from the secondary projectile. This remaining contribution of nuclear-induced fission can be subtracted if one assumes that it is identical to the appropriately weighted nuclear-charge distribution resulting from fission induced in the scintillator target, also accumulated under the condition on $Z_{cn} = 90$ in the corresponding charge-sum spectrum. In the following we describe how the weighting factor to be applied in the subtraction procedure was determined.

The intensities of the different peaks of the charge-sum spectra of fission events induced in the scintillator and in the lead target were determined by Gaussian fits. Figure 10 shows that the resulting intensities for both targets as a function of charge number follow a linear dependence in logarithmic representation. The slopes are slightly different for the two target materials. Since hydrogen is a component of the scintillation material, the difference in slope is in qualitative agreement with previous results on charge-changing cross sections reported in ref. [74], which showed a special behaviour of hydrogen-induced reactions. Only the peak at $Z = 90$ in the case of the lead target that is populated by electromagnetic excitations does not follow the linear dependence. Weak deviations for the neighbouring peaks probably result from non-Gaussian tails of the $Z = 90$ peak. The weighting factor to be applied was determined by extrapolating the logarithmic dependence of the relative charge-sum intensities as deduced from Figure 10 (lower part). The fission-fragment charge distribution that is obtained by subtracting the remaining part of nuclear-induced fission events is shown in Figure 9, lower part. This distribution represents the elemental yields after pure electromagnetic excitations. An analogous procedure was applied to the fission events of the other secondary projectiles investigated.

The condition on the charge-sum spectrum of the fission fragments also eliminates most events which suffer from secondary reactions in the different layers of matter in the beam line. In particular, all events in which the secondary projectiles undergo fragmentation reactions that change the nuclear charge in any layer upstream the target considered are suppressed. The same is true for all events in which the fission fragments lose any proton due to nuclear interactions downstream the target considered. This is extremely important since the probability

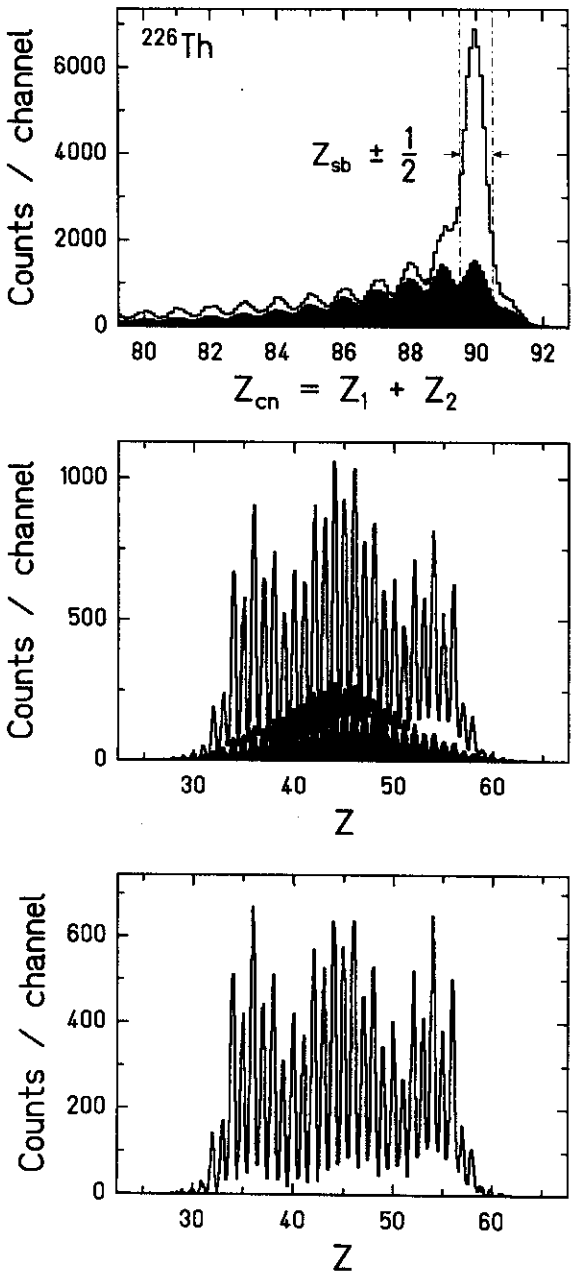

Figure 9: Upper part: Charge-sum spectrum of the fission fragments produced in the scintillator target (full histogram) and in the lead target (open histogram) from a ^{226}Th secondary beam. The condition on $Z = 90$ used in the further analysis is shown. The full histogram has been normalised in order to represent the fraction of nuclear-induced fission in the lead target at $Z = 90$ (see text). Middle part: Nuclear-charge response for fission fragments produced in the scintillation target (full histogram) and in the lead target (open histogram) from a ^{226}Th secondary beam. A condition on $Z = 90$ was imposed in the charge sum spectra (upper part). The full histogram has been normalised in order to represent the contribution of nuclear-induced fission in the lead target (see text). Lower part: Nuclear-charge response for fission fragments produced by electromagnetic excitations in the lead target from a ^{226}Th secondary beam. The spectrum was obtained as the difference of the two spectra shown in the middle part.

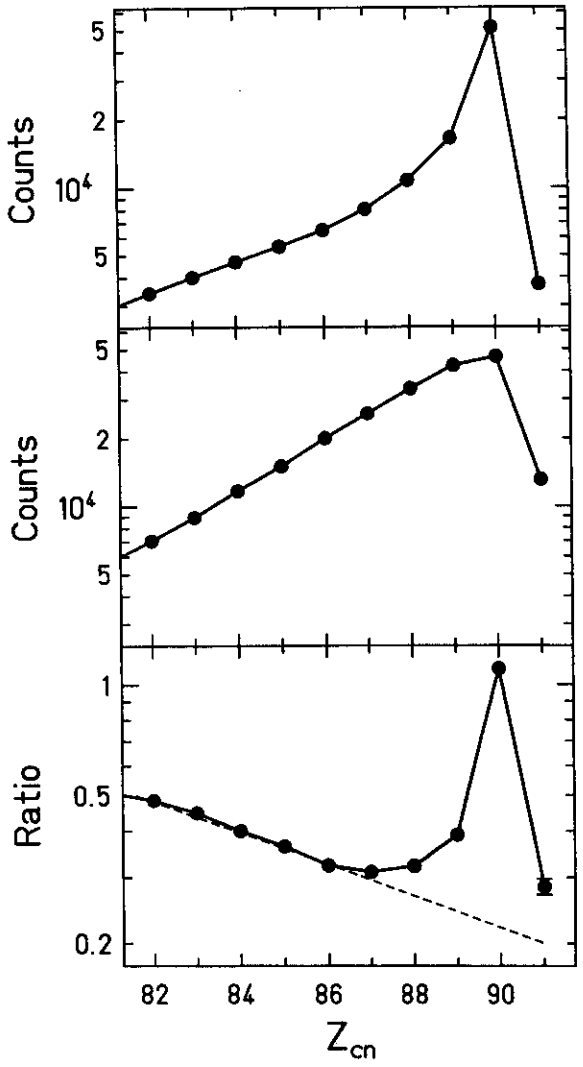

Figure 10: Intensities of the raw charge-sum spectra of the fission fragments produced in the lead target (upper part) and in the scintillator target (middle part) from a ^{226}Th secondary beam. The intensities corresponding to nuclear-induced fission can well be represented by straight lines in both cases. The lower part shows the ratio of the two upper spectra. The straight dashed line represents the estimated ratio of nuclear-induced fission from the two targets. Statistical error bars are smaller than the symbols.

that the secondary projectile or any of the fission fragments reacts in one of the layers in the beam line from the middle of the production target to the entrance of the time-of-flight wall (in addition to the fission in the lead target) amounts to 70 %! The condition on the charge sum allows to obtain an unperturbed experimental signature of electromagnetic-induced fission, in spite of the relatively large probability of multiple reactions. Finally, we stress that these layers are indispensable for the success of the experiment; all target layers, stripper foils and detectors as well as the energy degrader fulfil important tasks.

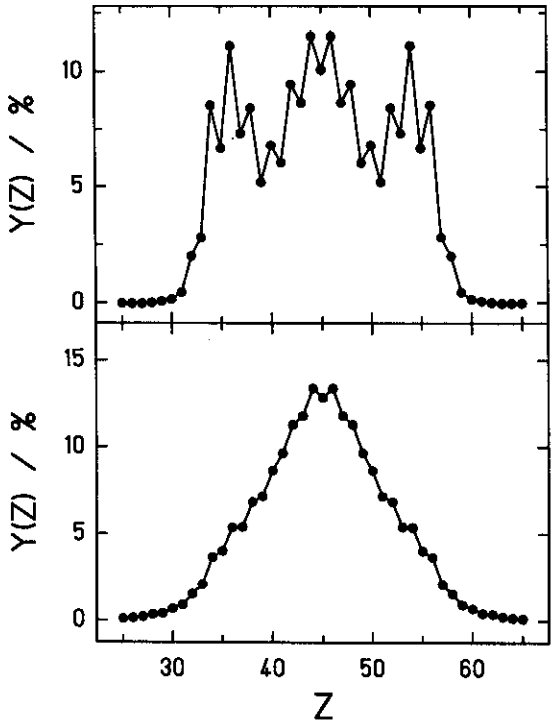

Figure 11: Element yields of fission products after electromagnetic excitation in a lead target (upper part) and after nuclear excitation in a plastic target (lower part) for a ^{226}Th secondary beam. A condition on $Z_1 + Z_2 = 90 \pm 1/2$ was imposed in both cases.

The element yields of the fission products emerging from electromagnetic excitations in the secondary lead target were extracted by determining the areas of the peaks in the spectra of the nuclear-charge response of the twin-MUSIC detector, corrected for the velocity dependence of the energy loss, shown in Figure 9, lower part. The elemental yields are shown in the upper part of Figure 11 for a ^{226}Th secondary beam.

In addition, the element yields of fission products emerging from nuclear interactions with the plastic target have been determined under the condition that the fission fragments contain all protons of the secondary projectiles. The corresponding spectrum, shown in Figure 11, lower part, is dominated by a broad symmetric component. As will be outlined below, these data correspond to a superposition of fission events from different thorium isotopes, extending to appreciably higher excitation energies.

In all cases, the elemental yields were found to be symmetric around $Z_{cn}/2$ within the expected statistical fluctuations. Note that any deviation from an exactly symmetric distribution is only possible due to the limited charge resolution. In order to minimise the statistical uncertainties, the charge distributions given in this paper are fully symmetrised. However, since the two fission fragments are strongly correlated due to the charge-sum condition imposed, the statistical error bars are calculated as the square root of the counting rates of the light fission products, only. The additional statistical uncertainties induced by the subtraction of the nuclear-induced fission events are taken into account.

2.6 Extraction of total kinetic energies

The total kinetic energy of the fission fragments was deduced from their velocity vectors, transformed into the centre-of-mass system of the fissioning secondary projectile. Since the fission fragments are detected with kinetic energies around 50 GeV each, a very high precision is required to determine the total kinetic energy of the fission products in the centre-of-mass system of the fissioning nucleus with the desirable accuracy of 1 MeV. In the following, the analysis procedure that is complicated by the slowing down in the different layers of matter is described in detail.

The magnetic rigidity of each secondary projectile in the second section of the spectrometer that is known with high precision (see above) served as a starting point of the analysis. Since nuclear charge and mass are known, this also defines the longitudinal velocity. By considering the energy loss in the layers of matter up to the target foil in which fission took place, the velocity $v_{sb}(z)$ of the secondary projectile along the flight path z was calculated. The energy-loss relations cited in ref. [68] were used. We also measured the time differences $TOF_{1,2}$ between the passage of the secondary projectile through the start detector, situated in front of the active target, and the arrival of both fission fragments in the time-of-flight wall, 5.5 m downstream (see Figure 4). From these measured time differences $TOF_{1,2}$, the time-of-flight of the secondary projectile t_{sb} from the start detector to the target foil in which fission took place was subtracted in order to obtain the time-of-flight values $t_{1,2}$ of the two fission fragments from the target foil to the time-of-flight wall. The time-of-flight of the secondary projectile was calculated as the integral $t_{sb} = \int 1/v_{sb}(z)dz$. (The time-of-flight of secondary projectile and fission fragments inside the target foil can be neglected.) The value of the velocity $v_{1,2}(z_{exit})$ at the exit of the target foil was determined for each fission fragment separately in an iterative procedure by matching the condition that the measured time-of-flight values $t_{1,2}$ are exactly reproduced by the integral $\int 1/v_{1,2}(z)dz$ from the target foil to the time-of-flight wall. Also here, the energy loss in the different layers of matter was taken into account. In these energy-loss calculations, estimated post-neutron-emission masses were used (see below). Finally, the condition of momentum conservation was applied in order to determine the depth inside the target foil where fission was induced. At this position, the velocity of the secondary projectile $w = v_{sb}(z_f)$ is required to be equal to the velocity $v_{cm}(z_f)$ of the centre-of-mass of the fission fragments with mass numbers $A_{1,2}$. This is formulated by the following equation:

$$v_{sb}(z_f) = v_{cm}(z_f) = \frac{A_1 \cdot v_1(z_f) + A_2 \cdot v_2(z_f)}{A_1 + A_2} \qquad (2)$$

Figure 12 demonstrates the kinematical conditions in detail. The difference in specific energy loss of secondary projectile and fission fragments gives the handle to determine the fission position in beam direction with a precision of 500 mg/cm^2 (FWHM).

The angle between the two fission fragments was deduced from the horizontal and vertical positions of the fission fragments measured in the twin MUSIC. From this angle, the transversal deflection angles of the individual fission fragments induced in the fission process were determined by again considering momentum conservation. The velocity vectors of the fission fragments in the laboratory system were then transformed into the centre-of-mass system of the secondary projectile in the moment of fission. A spectrum of the endpoints of these velocity vectors, projected onto the z-x plane, is shown in Figure 13. z denotes the direction of the beam, and x is the horizontal direction perpendicular to the beam. As expected, the spectrum shows a circular ridge with a radius of about 1 cm/ns, corresponding to the mean velocity of

the fission fragments in the centre-of-mass system. The spectrum is compatible with an isotropic emission of the fission fragments in the centre-of-mass system. The increased height of the ridge in backward direction is caused by the better velocity resolution due to the lower velocities of the backward-emitted fragments.

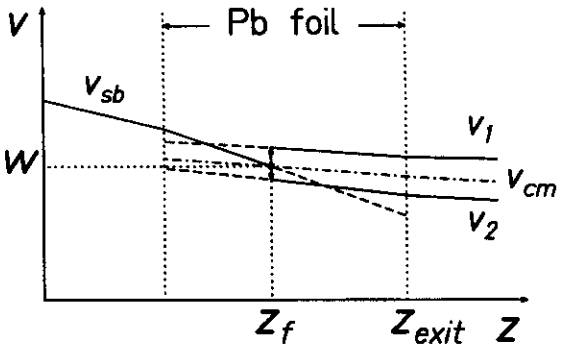

Figure 12: Schematic representation of the velocities of the secondary projectile (v_{sb}) and of the two fission fragments ($v_{1,2}$) in front, inside and behind the target foil. The position z_f of the fission reaction is determined by the condition of momentum conservation. Here the velocity of the secondary projectile $v_{sb}(z_f)$ is equal to the centre-of-mass velocity of the fission fragments $v_{cm}(z_f)$.

The mean pre-neutron-emission masses were estimated from the nuclear charges of the fragments by assuming the mass-to-charge ratio of the fissioning nucleus to be preserved. The total kinetic energy *TKE* of the two fragments was derived from the fragment centre-of-mass velocities and the pre-neutron-emission masses.

All data on total kinetic energies discussed in this work have been accumulated under the condition that the sum of the nuclear charges of the two fission fragments was equal to the nuclear charge of the secondary projectiles. As already mentioned, most events with additional interactions in the different layers of matter prior to fission were suppressed by this condition. The remaining contribution of such events was estimated to amount to less than 1 %. Two-dimensional representations of the total kinetic energies as a function of nuclear charge for fission of ^{233}U in lead and plastic are shown in Figure 14.

The total kinetic energies of the fission fragments resulting from pure electromagnetic-induced fission were deduced by disentangling the two possible processes, electromagnetic-induced and nuclear-induced fission, and their contributions to the two-dimensional *Z-TKE* spectra. Most fission events induced by nuclear interactions in the lead target are already suppressed by the condition that the number of protons of the secondary projectiles be preserved during fission. In order to remove the remaining contribution, the nuclear-induced fission events originating from the plastic target were subtracted from the events originating from the lead target in the two-dimensional *Z-TKE* spectra with the appropriate weight (see Figure 14). The procedure is analogous to that applied for the charge distributions, shown in Figure 9. The fraction to be subtracted is small (about 20%) for nuclei with high electromagnetic fission cross sections and amounts to 60 % for some of the less fissile nuclei. The statistical errors in the *TKE* values, introduced by this subtraction of nuclear background, are taken into account.

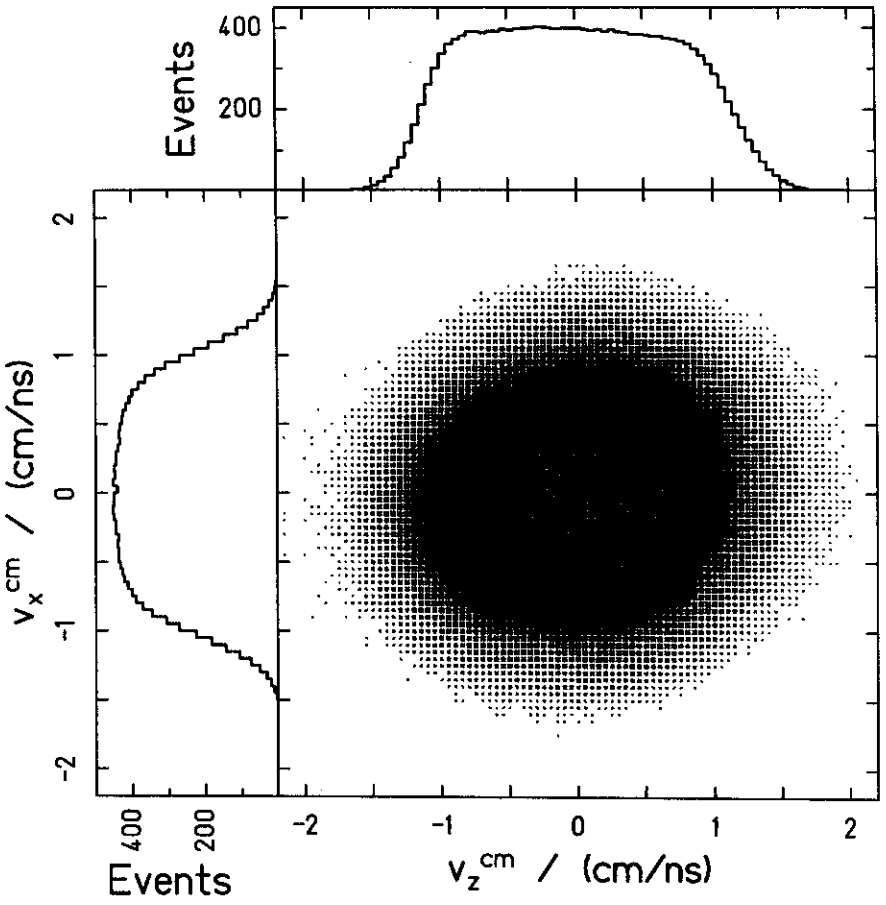

Figure 13: Two-dimensional spectrum of the endpoints of the measured velocity vectors of the fission fragments, transferred into the centre-of-mass system. The vectors have been projected on a plane defined by the beam direction *(z)* and the horizontal direction perpendicular to the beam *(x)*. In addition, the projections on the *x* and on the *z* axis are given.

Since the *TKE* values are deduced from time-of-flight and position measurements, they are determined on an absolute scale without any adjustment. From the precision of the calibrations of these quantities we estimate for the total kinetic energy a systematic error of 2 %.

Further considerations for the precision of the *TKE* values obtained with the analysis procedure described above include the influence of the number of neutrons lost before and after the fission process. Neutrons emitted prior to fission change the mass-to-charge ratio of the compound nucleus. This reduces the deduced *TKE* values by about 0.7 MeV per neutron removed. This causes a rather large uncertainty of a few MeV for nuclear-induced fission, where the loss of neutrons in the nuclear collision is large. The correction has to be estimated from a model calculation. However, it is negligible in the case of electromagnetic-induced fission where about 80% of the fission events originate from first-chance fission. The number of neutrons emitted from the fission fragments enters into the calculated mean energy loss of the

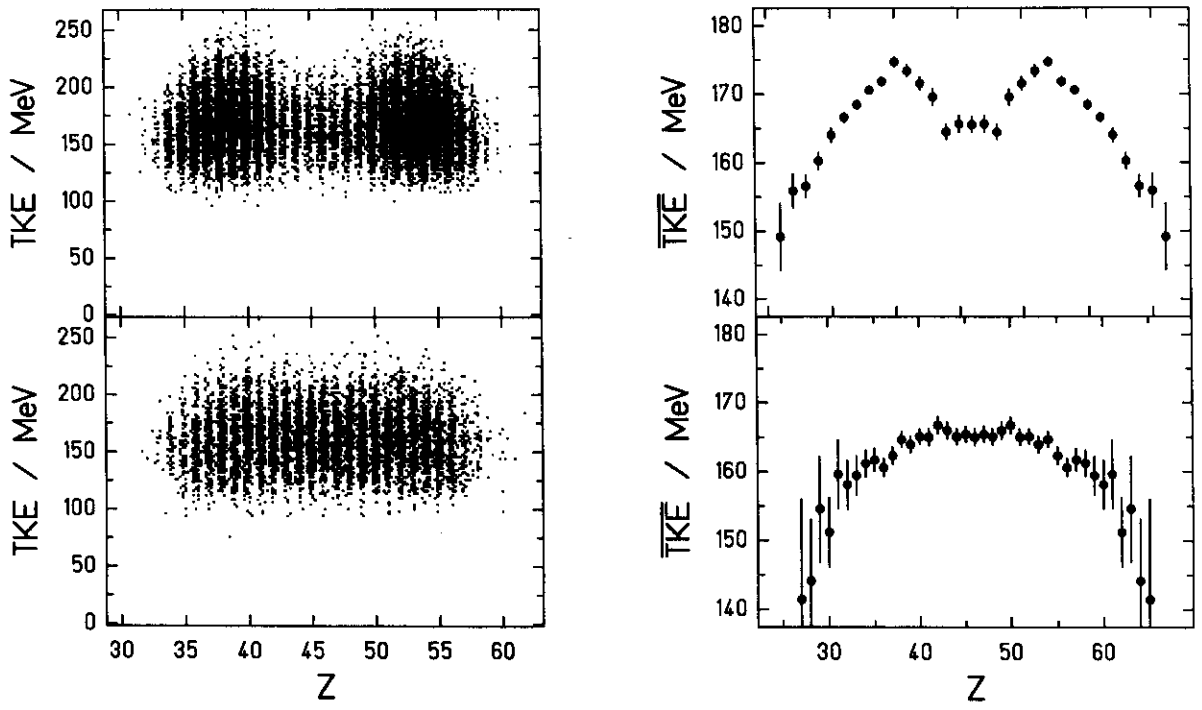

Figure 14: Two-dimensional representations of the total kinetic energy as a function of the nuclear charge of the fission fragments. The left figures show cluster plots, and the right figures show the mean values for every element. Upper part: The spectrum corresponds to fission of ^{233}U having passed the lead target at about 420 *A* MeV. The dominant part of 84% originates from electromagnetic-induced fission, while only 16% are due to nuclear collisions. Lower part: The spectrum corresponds to fission of ^{233}U induced by nuclear interactions with a plastic target. The width of the *TKE* distributions (left figures) is strongly influenced by the experimental resolution. The mean values, however, are determined with a precision of a few MeV (right figures).

fission fragments in the layers of matter between the two time-of-flight detectors. The influence of this number is rather weak. A variation of one unit in the total number of neutrons emitted from the fragments changes the *TKE* values by 0.1 MeV, only. The deformation of the fragments in the scission configuration is known to change the number of neutrons emitted from one fragment by about ± 1.5. This results in an uncertainty of the *TKE* values of about ± 1 MeV. Even this effect is small compared to the variation of the Coulomb energy at scission due to the influence of nuclear structure that amounts to more than 10 MeV. Thus, we conclude that the neutron number of the fissioning nucleus and those of the fission products that cannot be measured in our experiment do not crucially enter into the analysis which is aimed to yield information on the scission-point configuration. This is particularly important, since most of the systems investigated here have not been studied before, and the number of emitted neutrons can only be estimated from systematics. In our analysis we assumed that the fission fragments before neutron emission have the same *N/Z* ratio as the fissioning nucleus. The number of evaporated neutrons was assumed to amount to 3 in electromagnetic-induced fission and to 6.5 in nuclear-induced fission. They are attributed to the two fission fragments by equal parts. On the average, this is a reasonable assumption for low-energy fission where great part of the excitation energy of the fragments originates from deformation at scission. For nuclear-induced fission it would have been more realistic to attribute the excitation energy

to the two fragments according to the mass ratio; however, this would not change the results reported in this paper.

The resolution in *TKE* of a single event is limited by the time-of-flight resolution and by angular straggling of the fission fragments in the layers in front of the twin MUSIC. After transformation into the centre-of-mass system, both effects together lead to fluctuations of about 20 % (standard deviation) in the total kinetic energy, almost independent of the fission direction. Therefore, the dispersion of the total kinetic energy is dominated by the resolution, and the width induced in the fission process itself is difficult to obtain. Due to the limited resolution in the determination of the velocity vectors, the absolute *TKE* values are slightly overestimated. This is a general feature if a vector in three-dimensional space is determined with a statistical uncertainty. This effect was determined in a model calculation to amount to 2.3 MeV. The *TKE* values were corrected accordingly.

The rather large fluctuations in the measured *TKE* values due to the experimental conditions are connected to the inverse kinematics. In view of the large energies of about 50 GeV per fission fragment in the laboratory frame, the absolute resolution of about 40 MeV for one event corresponds to the high relative resolution of about 4×10^{-4}. However, mean *TKE* values can be determined with much higher accuracy, if the number of events recorded is sufficiently large. For the desirable accuracy of 1 MeV (standard deviation) for one charge split, more than 1000 events per charge split, that means several 10000 events in total have to be accumulated for one fissioning system. This estimate refers to statistical uncertainties which are decisive for revealing structural effects. Due to the high requirements on accuracy, the total kinetic energies will be discussed only for those cases that were measured with comparably high counting statistics.

3. EXCITATION ENERGIES INDUCED IN THE ELECTROMAGNETIC INTERACTION

The electromagnetic excitation in-flight of the radioactive-beam particles in the secondary target is one of the most important ingredients of the experiment, ideally adapted to the high beam energy. Although the excitation energy acquired is not precisely known for a single event, the excitation-energy distribution that is determined by the equivalent photon spectrum seen by the projectile and by the photo-absorption cross section of the projectile nucleus can be estimated on the basis of theoretical considerations and empirical systematics. The detailed knowledge of the excitation-energy distribution is important for the interpretation of the results.

In this section we investigate the excitation mechanism and discuss the conditions of the fission process. A similar analysis has been performed recently for the electromagnetic-induced fission of ^{238}U as reported in refs. [2,3,6]. The present study is primarily performed for two nuclei, ^{233}U and ^{234}U, for which comprehensive data on low-energy fission are available from previous experiments employing conventional techniques. In addition, it is intended to work out the general features that can be extended to the analysis of the variety of short-lived secondary projectiles studied in the present work. The isovector electric dipole resonance, including multi-phonon excitations, as well as the isoscalar and the isovector quadrupole resonances are considered. Excitations of magnetic resonances are neglected since they are assumed to be small. The basic features of electromagnetic excitations are treated as outlined in ref. [73]; however, several improvements were introduced as will be shown in the

following sections. We only give the relations and parameters that are necessary to document the calculations. A full description may be found in refs. [75,76,77,78,79].

3.1 Equivalent photon spectrum

The electromagnetic field of a lead nucleus of the secondary target seen by a projectile can be formulated as a flux of equivalent photons according to ref. [75]. Figure 15a) shows the spectrum of equivalent photons of the E1 and E2 electromagnetic fields seen by a projectile passing the secondary lead target at 430 *A* MeV. At the relativistic energies applied in the present experiment, the spectrum is hard enough to excite the giant resonances in the secondary projectiles.

3.2 Multi-phonon excitation of the giant dipole resonance

The nuclear absorption cross section $\sigma_{\gamma,\mathrm{E1}}(E)$ of the giant dipole resonance for a photon of energy E can be estimated from empirical systematics [76,77]. For the nuclei around mass number 220 studied in this work it can be described by a Lorentzian with a resonance energy of about $E_{\mathrm{E1}} \approx 79 \cdot A^{-1/3}\mathrm{MeV}$ and a width of about $\Gamma_{\mathrm{E1}} \approx 0.026 \cdot E_{\mathrm{E1}}^2\mathrm{MeV}^{-1}$. In deformed nuclei, the resonance splits into several components. The ratio of the resonance energies is reciprocal to the ratio of the main axes of the deformed nucleus, while the average energy of the absorption cross section remains unchanged. Figure 15b) shows that the estimated photoabsorption cross section of ^{234}U agrees quite well with experimental data.

Since the excitation cross section of the giant dipole resonance is high, a multiple excitation of this mode becomes non-negligible. We use the harmonic approximation outlined in refs. [78,79]. The energy-differential cross section for the excitation to an energy E in the passage of one target nucleus was calculated by the expression:

$$\frac{\mathrm{d}\sigma_{\mathrm{E1}}^{(1)}}{\mathrm{d}E}(E) = \sigma_{\gamma,\mathrm{E1}}(E) \cdot \int_{b_{\min}}^{\infty} e^{-P_{\mathrm{E1}}(b)} \frac{\mathrm{d}^2 N_{\mathrm{E1}}}{\mathrm{d}E\mathrm{d}S}(E,b) 2\pi b \mathrm{d}b \tag{3}$$

Here, $\frac{d^2 N_{\mathrm{E1}}}{\mathrm{d}E\mathrm{d}S}$ is the flux of equivalent photons per energy interval and unit area seen by the projectile. The mean number $P_{\mathrm{E1}}(b)$ of excitations of the giant dipole resonance in the projectile for a trajectory with an impact parameter b was calculated by:

$$P_{\mathrm{E1}}(b) = \int_0^{\infty} \frac{d^2 N_{\mathrm{E1}}}{\mathrm{d}E\mathrm{d}S}(E,b) \sigma_{\gamma,\mathrm{E1}}(E) \mathrm{d}E \tag{4}$$

For the sake of simplicity, the "sharp-cut-off" approximation was applied. The minimum impact parameter for which only electromagnetic interaction occurs was taken from ref. [72] as proposed in ref. [80]:

$$b_{\min} = r_0\left[A_P^{1/3} + A_T^{1/3} - x\left(A_P^{-1/3} + A_T^{-1/3}\right)\right] \tag{5}$$

with r_0 = 1.34 fm and x = 0.75. It has been shown in ref.[80] that the calculations with the sharp-cut-off approximation produce nearly identical results to a more elaborated microscopic approach.

In the case of the absorption of two photons, one obtains the following expression:

$$\begin{aligned}\frac{d\sigma_{E1}^{(2)}}{dE}(E) &= \frac{1}{2}\int_{b_{\min}}^{\infty} e^{-P_{E1}(b)}\, 2\pi b\, db \\ &\cdot \int_0^E \frac{d^2N_{E1}}{dE\,dS}(E',b)\,\sigma_{\gamma,E1}(E')\,\frac{d^2N_{E1}}{dE\,dS}(E-E',b)\,\sigma_{\gamma,E1}(E-E')\,dE'\end{aligned} \tag{6}$$

The absorption of more than two photons is rather unlikely and thus could be neglected.

In recent experiments, the cross section for the two-phonon excitation of the giant dipole resonance has been investigated for heavy nuclei. An enhancement of the measured cross section by a factor of 1.3 was found for ^{208}Pb compared to the calculations in the harmonic approximation in ref. [81]. In contrast, the measurements for ^{238}U coincide with the calculations [2]. In our calculations we used the harmonic approximation without any enhancement.

3.3 Giant quadrupole resonances

The nuclear absorption cross sections $\sigma_{\gamma,E2}^{(i)}(E)$ of the isoscalar (i=1) and of the isovector (i=2) giant quadrupole resonances for a photon of energy E were derived from empirical systematics [82,83,84]. For the nuclei studied here, the isoscalar and the isovector mode have a resonance energy of about $E_{E2}^{(1)} \approx 64.7 \cdot A^{-1/3}$MeV and $E_{E2}^{(2)} \approx 130 \cdot A^{-1/3}$MeV, respectively, and a width of $\Gamma_{E2}^{(1)} \approx 17.5 \cdot A^{-1/3}$MeV and $\Gamma_{E2}^{(2)} \approx \left(10.5 - 0.073 \cdot A^{2/3} - 0.00174 \cdot A^{4/3}\right)$MeV, respectively. The energy-differential cross section for the excitation to an energy E in the passage of the target were calculated by the expression:

$$\frac{d\sigma_{E2}}{dE}(E) = \frac{dN_{E2}}{dE}\left(\sigma_{\gamma,E2}^{(1)}(E) + \sigma_{\gamma,E2}^{(2)}(E)\right) \tag{7}$$

Multiple excitations of the quadrupole resonances were neglected.

3.4 Excitation energies at fission

The excitations induced in the secondary ^{234}U projectiles resulting from the electromagnetic interaction with the lead target nuclei populate an energy distribution $d\sigma / dE$ (Figure 15c) that peaks at about 11 MeV near the lower peak of the giant dipole resonance. The high-energy part of the nuclear absorption cross section (Figure 15b) is strongly suppressed due to the equivalent photon spectrum that steeply decreases with energy (Figure 15a).

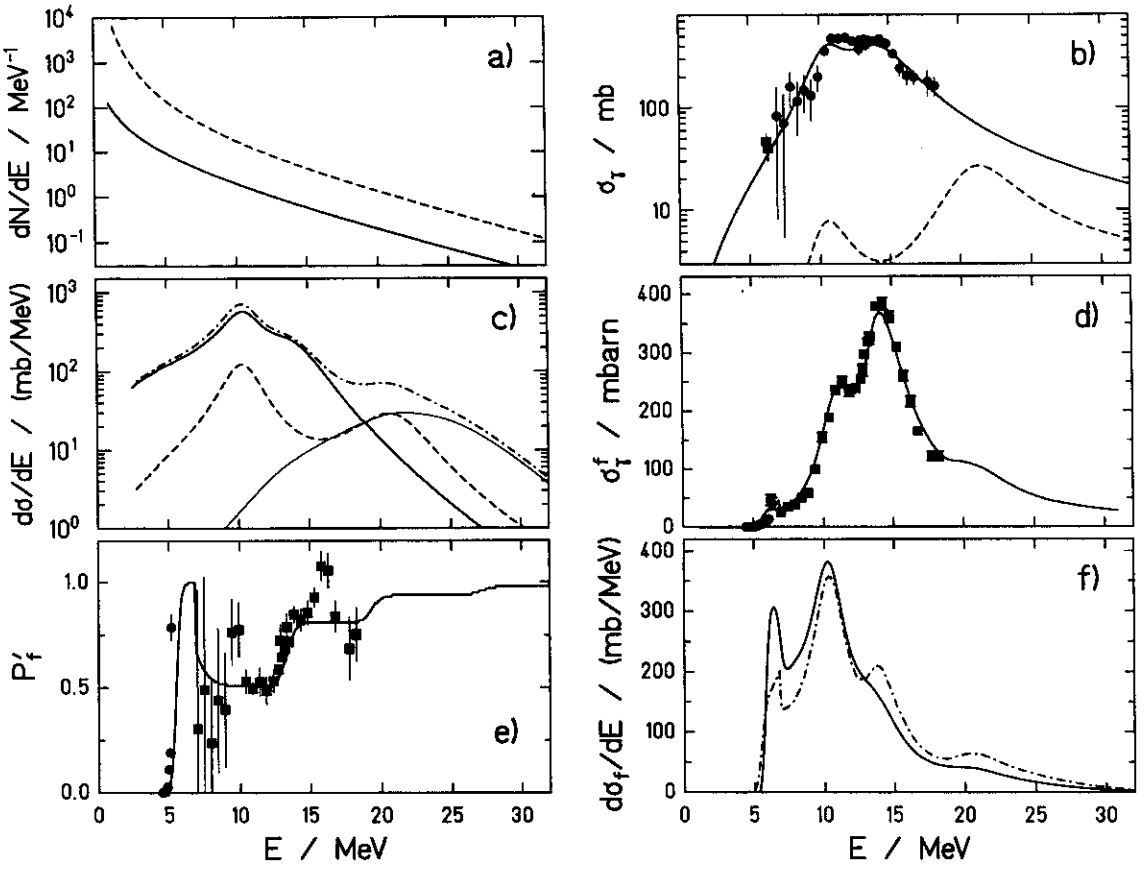

Figure 15: Evaluation of the energy-differential fission cross section for the reaction ^{234}U on ^{208}Pb at 430 *A* MeV. (a) Calculated spectrum of equivalent photons for the E1 (full line) and E2 (dashed line) electromagnetic fields seen by the projectile. (b) Calculated absorption cross section of ^{234}U for E1 (full line) and E2 (dashed line) radiation. The points represent measured data on E1 absorption cross sections from refs. [85,86]. (c) Calculated excitation-energy distribution of ^{234}U projectiles after one-phonon E1 (full line) and E2 (dashed line) electromagnetic excitations in the lead target. The thin full line denotes the two-phonon excitation of the giant dipole resonance. The total absorption cross section is also shown as a dash-dotted line. (d) Calculated (full line) and measured [85,86] (data points) electromagnetic fission cross section of ^{234}U for E1 excitations. (e) Calculated (full line) and measured [85,86] (data points) fission probability of ^{234}U, including fission after neutron evaporation. (f) Calculated energy-differential fission cross section $d\sigma^f / dE$ (dash-dotted line) after electromagnetic excitation of ^{234}U in a lead target at 430 *A* MeV, resulting from the product of the curves in a), b), and e) and calculated distribution of excitation energies $d\sigma^f / dE_f$ of uranium isotopes at fission after electromagnetic excitation of ^{234}U (full line). The last curve differs from $d\sigma^f / dE$ by the reduction in excitation energy due to neutron evaporation prior to fission: E is the excitation energy acquired in the electromagnetic interaction and E_f is the excitation energy at fission. Note that the labels E_f and $d\sigma^f / dE_f$ at the axes of part f) are omitted. For more details see text.

Excitations that exceed the fission barrier may lead to fission. However, also neutron evaporation has to be considered as the most important competing deexcitation channel. First, its competition determines the energy-dependent fission probability $P_f(E)$ and, secondly, it populates neighbouring isotopes at lower excitation energies that may also contribute to fission. In the case of ^{234}U, fission events induced by electromagnetic excitations are composed of about 80 % first-chance fission (^{234}U), 15 % second-chance fission (^{233}U) and a small fraction of higher-chance fission (mostly ^{232}U) according to our calculations. The conditions for the other secondary beams are expected to be similar. The measured fission properties always represent a mixture of about 3 isotopes. However, first-chance fission dominates strongly. In Figure 15d) and e), the photo-fission cross section σ_γ^f and the fission probability P_f used in our calculation which both include multi-chance fission are compared to measured data.

The distribution $d\sigma^f / dE$ of primary excitation energies leading to fission that is given by the product of $d\sigma / dE$ and P_f is shown in Figure 15f). It does not yet represent the excitation energies at fission. This is the distribution $d\sigma^f / dE_f$, also shown in Figure 15f), which includes the reduction in excitation energy due to neutron evaporation prior to fission.

The calculation of the fission probability was performed with a constant-temperature formalism as described in ref. [73]. No direct decay of the giant resonances was considered. It was assumed that the deexcitation always proceeds via the formation of a compound nucleus. For the system ^{234}U, the calculated values are in good agreement with measured data from photo fission [85,86], see Figure 15d).

We extended the study also to ^{233}U. The results are not shown, since also for this nucleus, the measured data [86] could be well reproduced.

For most of the more neutron-deficient secondary projectiles, no data exist on the excitation-energy dependent fission probabilities. Therefore, we only give the calculated excitation-energy distributions after electromagnetic excitation of two other secondary projectiles in a lead target at $E = 430\ A$ MeV in Figure 16. The parameters used in the calculation are taken from the systematics described above. As expected, the excitation-energy distributions are all rather similar to each other, in spite of the slight mass-dependence of the resonance energies and the deformation-dependent splitting of the GDR. Therefore, the drastic variations of the structural effects found for the different systems as presented below cannot be explained by variations in the excitation-energy distribution.

4. EXCITATION ENERGIES INDUCED IN NUCLEAR INTERACTIONS

For completeness, we also give the excitation-energy distribution at fission after nuclear collisions of ^{234}U inside the plastic target, calculated with the ABRABLA code [87,88] under the condition that all protons of the secondary projectile are still present in the fission fragments. This condition selects very peripheral collisions that only remove neutrons from the secondary projectile. As Figure 17 shows, the distribution of excitation energies at fission is broad with a mean value of 27 MeV. Multi-chance fission is important: The average mass of fissioning uranium isotopes is 231.7, corresponding to a mass loss of $\Delta A = 2.3$ prior to fission. The conditions are again expected to be similar for the other secondary beams studied.

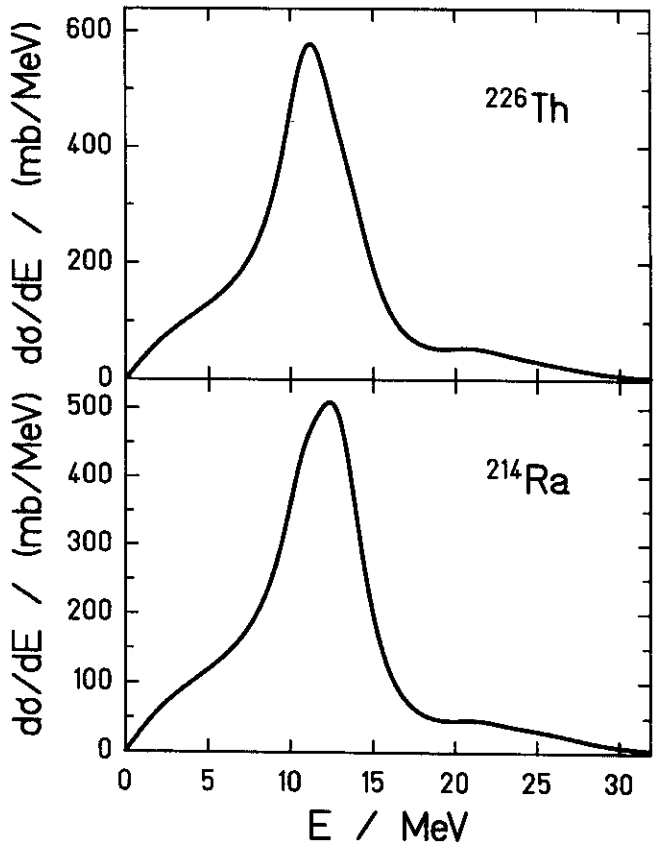

Figure 16: Calculated excitation-energy distributions of ^{226}Th and ^{214}Ra used as secondary projectiles after electromagnetic excitations in a lead target at 430 A MeV.

5. ^{233}U AND ^{234}U: TWO TEST CASES

As discussed in the preceding chapters, the excitation mechanisms applied in the present work, electromagnetic and nuclear interactions in-flight, lead to excitation-energy distributions. Therefore, the data of the present work cannot directly be compared to previous results of other experiments. The systematic deviations of preliminary results for ^{233}U of the present experiment from previous data acquired in thermal-neutron-induced fission of ^{232}U have already been shown in a letter [65]. In Figure 18, we give the corresponding final results for the two nuclei ^{233}U and ^{234}U. While the gross features of both the nuclear-charge distribution and the total kinetic energies are very similar in electromagnetic and in thermal-neutron-induced fission, some quantitative differences can be observed: The yields near symmetry are appreciably higher, and the even-odd structure is reduced by almost a factor of two if compared to the data from thermal-neutron-induced fission. In addition, the total kinetic energies near symmetry for ^{233}U are larger by about 5 MeV. These differences can qualitatively be explained by the higher excitation energies populated in the electromagnetic interaction (see Figure 15), in particular by the tail extending to about 20 MeV. When interpreting the data of the present work, the effect of the excitation-energy distribution has to be taken into account. In the following, we will quantitatively discuss the peak-to-valley ratio and the global even-odd effect.

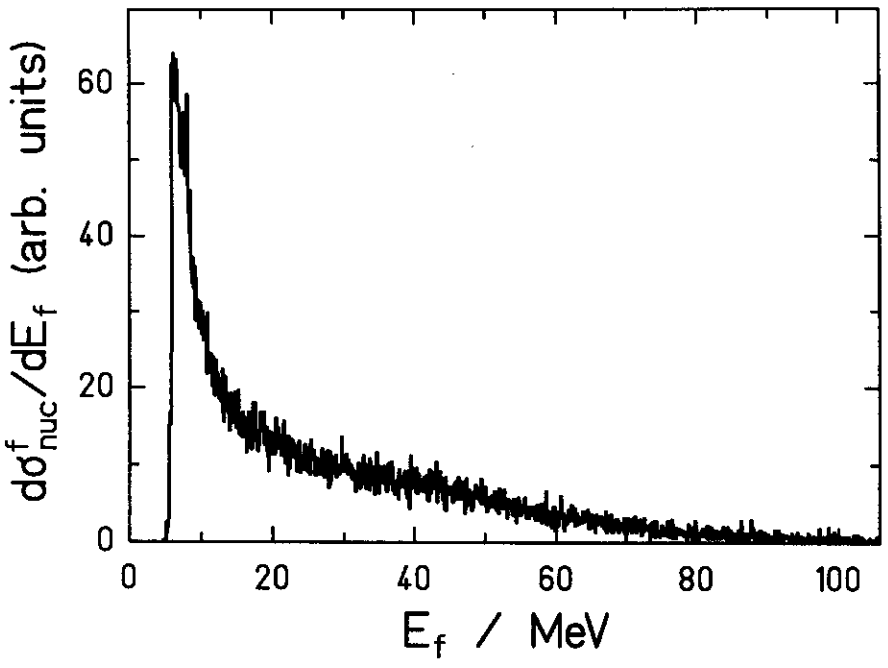

Figure 17: Calculated distribution of excitation energies at fission after nuclear collisions of ^{234}U in the plastic target. Only peripheral collisions that did not remove any protons from the secondary projectile are considered.

For nuclei with a weak symmetric fission component, the peak-to-valley ratio of the element or mass distributions is an important characteristic quantity. When comparing peak-to-valley ratios obtained in the present experiment with those measured at fixed excitation energies, the excitation-energy distribution has to be considered appropriately. Peak-to-valley ratios are usually determined as a function of the initial excitation energy E, which may be different from the excitation energy E_f at fission; see discussion of Figure 15. When the energy-dependent relative yield in the peak at asymmetry is denoted by $Y_{Peak}(E)$ and the yield in the symmetric valley is denoted by $Y_{Valley}(E)$, the peak-to-valley ratio $\langle Y_{Peak} / Y_{Valley} \rangle$, observed for an excitation-energy distribution $P(E)$, is given by:

$$\left\langle \frac{Y_{Peak}}{Y_{Valley}} \right\rangle = \frac{\int Y_{Peak}(E) \cdot P(E) \mathrm{d}E}{\int Y_{Valley}(E) \cdot P(E) \mathrm{d}E} \tag{8}$$

As usual, the yields measured at each excitation energy are normalised: $\sum_Z Y(Z) = 200\%$. The effective excitation-energy distribution $P(E)$ is given by the normalised excitation-energy-dependent fission cross section $\mathrm{d}\sigma_f / \mathrm{d}E$, as defined above. Note that formula (8) differs from the approximate treatments applied by Armbruster et al. [3] and by Rubehn et al. [6].

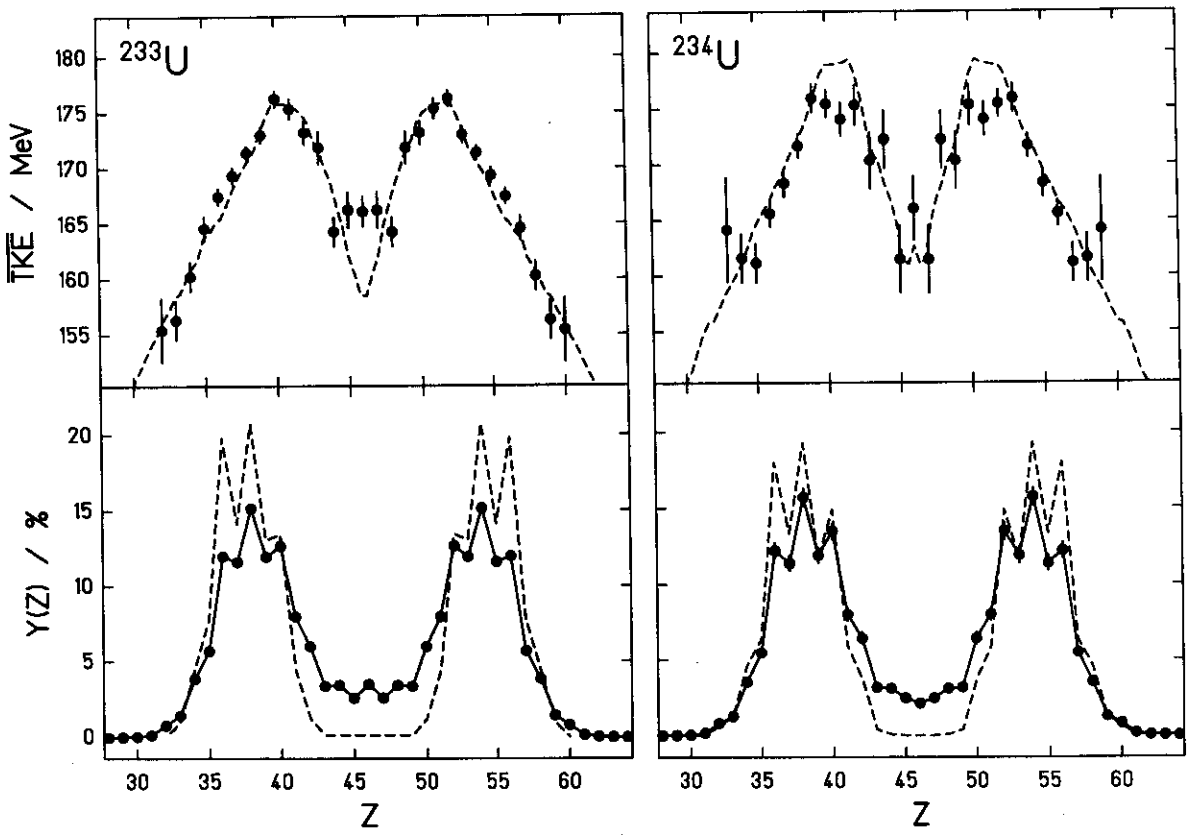

Figure 18: Comparison of electromagnetic-induced with thermal-neutron-induced fission. Upper parts: Mean total kinetic energies as a function of the fission-fragment charge for electromagnetic-induced fission of ^{233}U(left) and ^{234}U(right) in a lead target (data points) compared to data from ref. [89] (dashed lines) for *TKE* as a function of fragment mass for ^{232}U(n_{th},f) and ^{233}U(n_{th},f). The mass scale of the data from thermal-neutron-induced fission is adapted to the charge range. Lower parts: Nuclear-charge yields for electromagnetic-induced fission of ^{233}U (left) and ^{234}U (right) in a lead target (data points) and from refs. [90] and [54] (dashed lines) for ^{232}U(n_{th},f) and ^{233}U(n_{th},f), respectively. For the present data, only the statistical errors are shown. The *TKE* values of the present work are subject to an additional systematic uncertainty of 2%.

When the peak-to-valley ratio is averaged over energy as was done in ref. [6] or when the peak-to-valley ratio is taken at the mean excitation energy as was done in ref. [3], this will in general lead to different results. For the even-odd effect δ, the averaging over the excitation-energy distribution can be formulated in the following way:

$$\langle \delta \rangle = \int \delta(E) \cdot P(E) \mathrm{d}E \qquad (9)$$

where $\delta(E)=\left(\sum_{evenZ} Y(E)-\sum_{oddZ} Y(E)\right)/\sum_{allZ} Y(E)$ denotes the excitation-energy-dependent global even-odd effect. Again, the even-odd effect taken at the mean excitation energy would not yield the correct result.

In Table 3 we compare the peak-to-valley ratio and the proton even-odd effect measured in the present work for ^{233}U and ^{234}U with expectations based on other data and on theoretical predictions. The measured peak-to-valley ratio has been determined with the even-odd structure in the elemental yields averaged out. The expected values have been calculated with Eq. (8) and Eq. (9), respectively. They are given for ^{234}U only. These values are considered to be valid for ^{233}U too, since the uncertainty of the calculation is larger than any expected difference between the values of these two nuclei. Relevant parameters used in the calculation are listed in Table 4. Similar comparisons have been made in refs. [3,6] for electromagnetic-induced fission of ^{238}U, however, due to the approximations applied there, the results cannot directly be compared.

The excitation-energy-dependent relative yields Y_{peak} and Y_{valley} were parameterised in accordance with data of the compound systems ^{234}U , ^{239}U, ^{233}Th, ^{236}U, ^{240}Pu, and ^{233}Pa, see Figure 19. The lines shown in Figure 19 represent the dependencies used in the calculation. It was assumed that the peak-to-valley ratio in the mass yields is identical to that in the charge yields. The peak-to-valley values found in this experiment are much smaller than the expected ones, see Table 3. This could be an indication that the electromagnetic interaction populates higher excitation energies more strongly than expected. However, even if the two-phonon excitation of the giant dipole resonance is enhanced by a factor of 4, the data cannot yet be reproduced. This is why the explanation for this discrepancy is probably to be found somewhere else. An additional high-energy component which would decrease the peak-to-valley ratio by a factor of two would correspond to about 5% of the total fission cross section. May be that interference effects between nuclear and electromagnetic interactions which are usually neglected are responsible for such a contribution. One could also take into consideration that the method illustrated in Figure 10 does not completely subtract the background of fission events after nuclear excitation. In addition, our calculation of the expected peak-to-valley ratio is rather uncertain since it relies on a common fit to five different fissioning systems. It seems that the problem of the reduced peak-to-value ratio cannot be solved on the basis of the present data.

The excitation-energy-dependent proton even-odd effect $\delta(E)$ has been estimated by use of the analytic relation given in ref. [91], which is based on experimental data for ^{238}U:

$$\delta(E)=\begin{cases}\delta_0 & \text{for } E < B_f + 2\Delta \\ \delta_0 \cdot \mathrm{e}^{-\frac{E-B_f-2\Delta}{T}} & \text{otherwise}\end{cases} \qquad (10)$$

with 2Δ =2.15 MeV and T = 1 MeV. In addition, the empirical parameterisation from ref. [92] with a modified parameter T = 1.6 MeV and the theoretical expectation from ref. [93] have been used. The latter formulates the probability of a completely paired proton configuration at scission in the framework of the super-fluid nuclear model and predicts an even more gradual decrease of the proton even-odd effect with excitation energy. The plateau value of the proton even-odd effect δ_0 = 22.1% was taken from data on thermal-neutron-induced fission of ^{233}U (ref. [54]). The values given in Table 3 show that our data are rather close to the theoretical expectation but differ strongly from the systematics. However, it is probably too early for a

final conclusion. On the one hand, the measured data, the systematics [91,92] is based on, have rather large error bars, and on the other hand, the theoretical calculation is rather sensitive to a few parameters, e.g. the values of the fission barriers, which are not precisely known neither. In any case, the surviving of pairing correlations in fission remains a subject of interest to be studied more precisely.

Table 3: Characteristic quantities of the element distributions for fission fragments of ^{233}U and ^{234}U. Upper part: The peak-to-valley ratios P/V and the proton even-odd effects δ measured in the present work are compared to calculated values that have been obtained by averaging over the calculated excitation-energy distribution. a) The energy distribution after electromagnetic excitation from Figure 15c) was used. b) The probability for 2-phonon-excitations was increased by a factor of 4. Lower part: The expected value of the even-odd effect has been calculated with different options for the excitation-energy dependence of the even-odd effect: c) empirical parameterisation from ref. [91], d) empirical parameterisation from ref. [92], e) theoretical prediction from ref. [93].

Nucleus	^{233}U	^{234}U
<P/V> (exp)	4.5 ± 0.5	6.0 ± 1.4
<P/V> (calc) a)		11.1
<P/V> (calc) b)		7.3
$<\delta>$ (exp)	(10.9 ± 0.6) %	(12.5 ± 1.5) %
$<\delta>$ (calc, T = 1 MeV) c)		5.4 %
$<\delta>$ (calc, T = 1.6 MeV) d)		6.6 %
$<\delta>$ (calc, microscopic) e)		9.1 %

Table 4: Relevant parameters of ^{231}U to ^{234}U used in the calculations. Fission barriers B_f are averaged values from experimental data [94], neutron binding energies B_n are taken from ref. [95], and fission probabilities are deduced from refs. [96,66].

Nucleus	^{231}U	^{232}U	^{233}U	^{234}U
B_f	5.6 MeV	5.6 MeV	5.6 MeV	5.6 MeV
B_n	5.90 MeV	7.25 MeV	5.76 MeV	6.84 MeV
P_f	0.80	0.72	0.60	0.49

In summary, we state that the comparison of the charge-yield distributions after electromagnetic-induced fission of ^{233}U and ^{234}U with data from thermal-neutron-induced fission shows that the general characteristics of the nuclear-charge distributions and of the total kinetic energies of the fission fragments are similar. The deviations are qualitatively expected due to the higher excitation energies involved in electromagnetic excitations. However, the

peak-to-valley ratio and the even-odd effect cannot quantitatively be understood on the basis of previously measured data of the excitation-energy dependence of these characteristic quantities. Still, the data available from literature are too uncertain to draw any final conclusion. The detailed analysis given in this chapter gives the necessary guideline for the interpretation of the new results acquired in the present experiment in comparison with previously measured data.

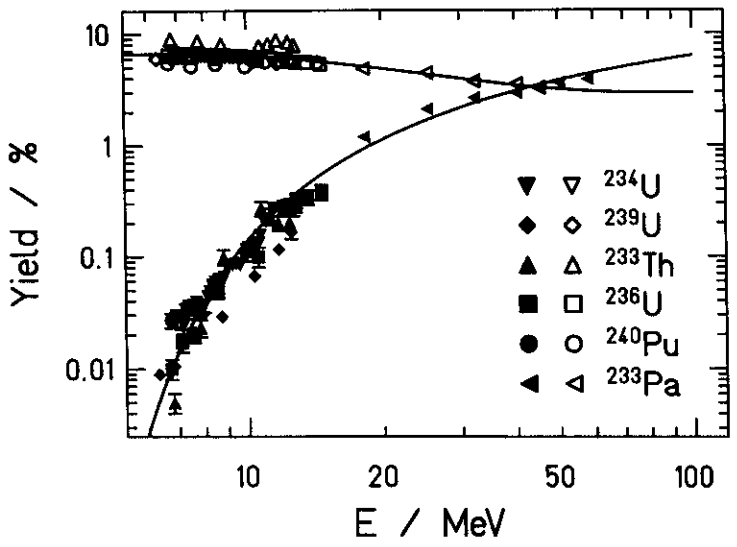

Figure 19: Mass yields for A ≈ 140, near the peak of the asymmetric component, (open symbols) and at symmetry (full symbols) as a function of excitation energy for several systems as measured in previous experiments (^{233}U(n,f), [97], ^{238}U(n,f) [98], ^{232}Th(n,f) [99], ^{235}U(n,f) [100], ^{239}Pu(n,f) [101], ^{232}Th(p,f) [102]) The compound nuclei formed in the reactions are indicated. The lines represent analytical fit functions (see text).

6. RESULTS

In the present experiment, the elemental yields and the total kinetic energies for a series of neutron-deficient pre-actinides and actinides from ^{205}At to ^{234}U have been determined. An overview on these results is given in Figure 20 and Figure 21. The elemental yields after electromagnetic-induced fission, covering the transition from symmetric fission at ^{221}Ac to asymmetric fission at ^{233}U, are shown in the upper part of Figure 20. In the transitional region, around ^{227}Th, triple-humped distributions appear, demonstrating comparable weights for symmetric and asymmetric fission. The lower part of Figure 20 shows the elemental yields for lighter nuclei reaching from ^{205}At to ^{221}Th. In all these cases symmetric fission prevails. The total kinetic energies that were determined with sufficient counting statistics are depicted in Figure 21. These show very clear signatures of nuclear structure as well. These new data now systematically fill the gap between the regions of symmetric and asymmetric fission shown in Figure 1.

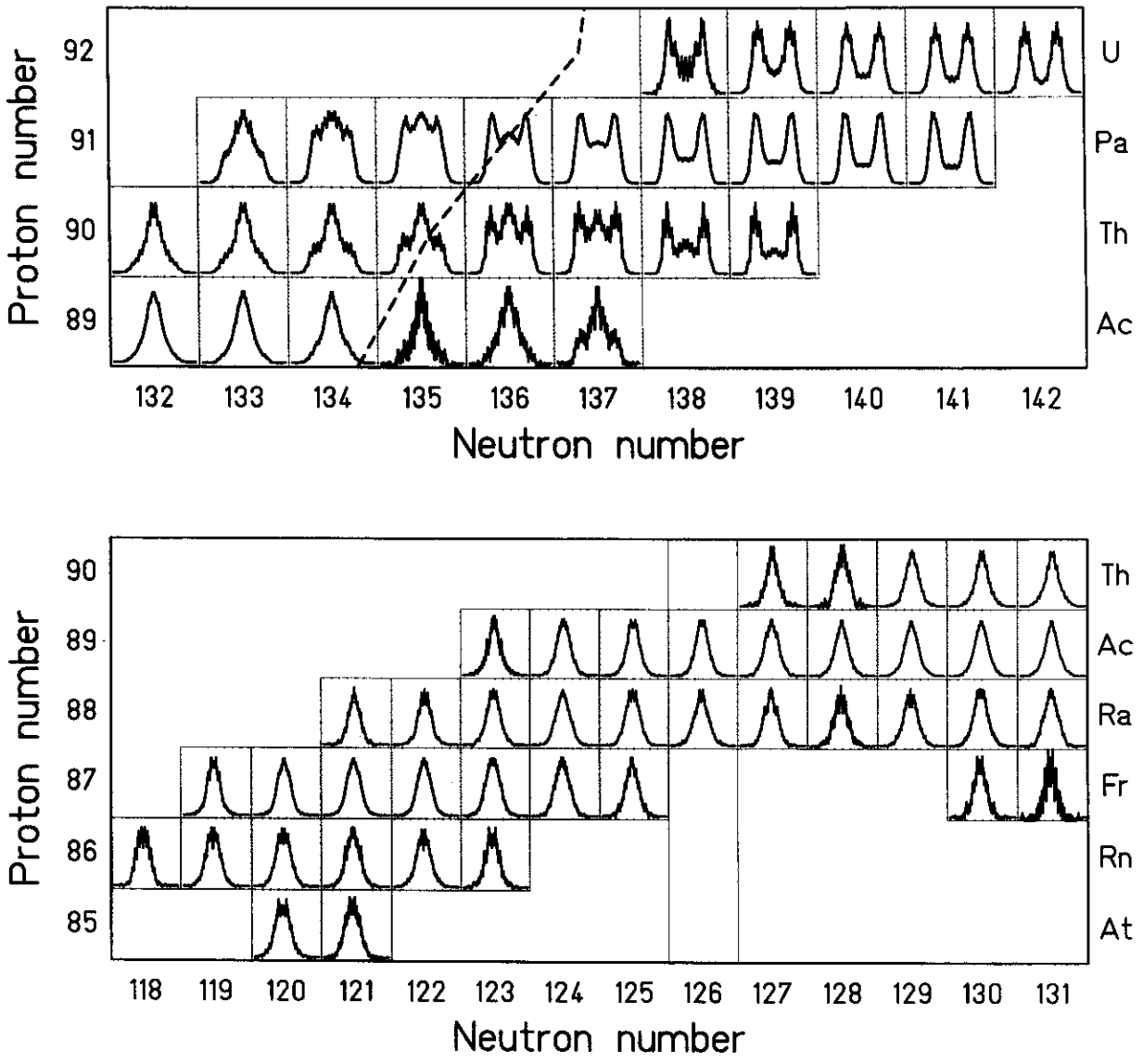

Figure 20: Measured fission-fragment nuclear-charge distributions in the range Z = 24 to Z = 65 from ^{221}Ac to ^{234}U (upper part) and from ^{205}At to ^{221}Th (lower part) in electromagnetic-induced fission are shown on a chart of the nuclides. The dashed line in the upper part indicates the transition from symmetric to asymmetric fission as predicted by Möller [103] who calculated the stability of the saddle-point configuration against mass-asymmetric deformations. Nuclei on the right-hand side of this line were expected to predominantly show asymmetric fission, while nuclei on the left-hand side were expected to show symmetric fission with higher probability.

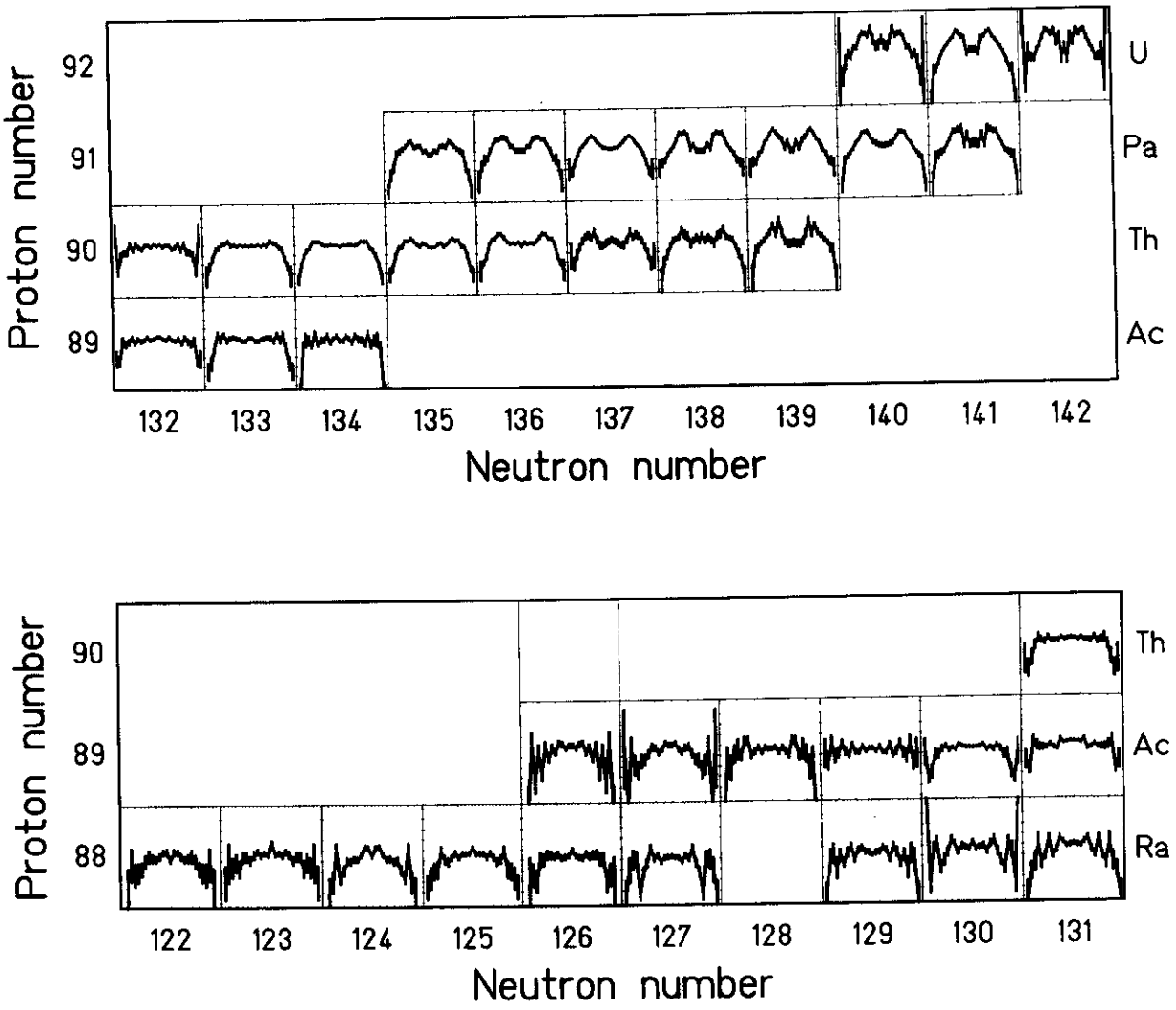

Figure 21: Measured mean total kinetic energies as a function of the fission-fragment nuclear charge in the range Z = 31 to Z = 59 in electromagnetic-induced fission for the secondary beams ^{221}Ac to ^{234}U (upper part) and ^{210}Ra to ^{221}Th (lower part) are shown on a chart of the nuclides.

The data allow to follow the mean charge split in the asymmetric fission component over long isotopic chains. Figure 22 shows the mean positions of the heavy charge peak. It reveals that the heavy asymmetric fission component is centred at proton number 54 for all systems investigated. Also the mean mass and neutron numbers of the asymmetric peaks were deduced from the measured elemental yields by applying the unchanged-charge-density (UCD) assumption. Both the mass and the neutron number vary over several units. This is a surprising result, since the asymmetric fission component is usually traced back to the influence of neutron shells in the heavy component (e.g. [11]). This remarkable finding puts an important constraint on the theoretical description of the fission process. It deserves a careful discussion on the basis of elaborate fission models. It is not clear at this moment, whether shell effects in

proton number play a decisive role for the charge split of the systems or whether the constant position in proton number is a fortuitous result of more complex relations.

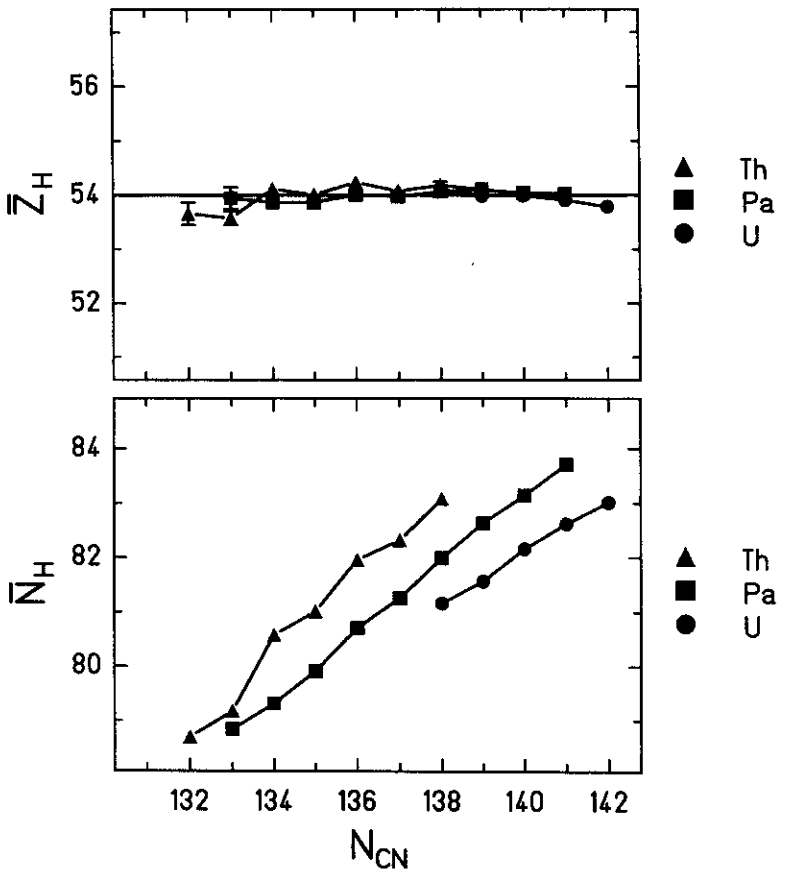

Figure 22: Mean position of the heavy asymmetric component in charge number (upper part) and neutron number (lower part) for those nuclei for which an asymmetric component was observed. The data refer to electromagnetic-induced fission. In the upper part, a horizontal line is given for $Z = 54$ in order to illustrate the constant mean proton number of the heavy component. While the charge number is measured, the neutron number is estimated by the UCD assumption: $N_H = Z_H N_{CN}/Z_{CN}$, thus neglecting any polarisation effects.

The weights of the two fission components, the symmetric and the asymmetric one, were quantitatively determined by fitting three Gaussian curves to the charge-yield distributions, one for the symmetric component and two others for the light and the heavy peak of the asymmetric component. In those cases where either the asymmetric or the symmetric component was too weak, the position and the width of the asymmetric components or the width of the symmetric component, respectively, were imposed to the fit. In the case of a weak symmetric component, the width of this component was fixed to 9.5 charge units (FWHM), corresponding to a standard deviation of 4.04 charge units. This value was deduced from the systematics shown in Figure 24. Also guided by the systematics of Figure 24, the width of the asymmetric component was fixed to 4.7 charge units (FWHM), corresponding to a standard

deviation of 2.13 charge units, for the more neutron-deficient isotopes. The mean position of the heavy asymmetric component was fixed to $Z = 54$ in these cases, following the systematics of Figure 22. The strengths of the symmetric and of the asymmetric fission components were then determined by the areas of the Gaussians describing the data. The numerical results are given in Table 5.

The resulting values of the ratio of symmetric to asymmetric fission are shown in Figure 23. Data obtained from fission after fusion reactions are included for comparison [27,32]. They show higher yields of the symmetric component. This may be attributed to the higher excitation energies involved. The transition from symmetric to asymmetric fission is steep but rather smooth. For all nuclei with $A < 226$, the symmetric component has been found to prevail. When compared to neutron number or charge number of the fissioning nucleus, the mass number turned out to be by far the best suited ordering parameter. The same has already been suspected by Specht [30] for nuclei in the mass region $A = 225$ to 236. The decisive influence of the mass number is surprising, since the origin of the asymmetric fission is attributed to shell effects in the nuclear neutron and proton subsystems, where the most important role is attributed to the spherical $N = 82$ and the deformed $N = 88$ shells [11]. Strutinski-type potential-energy calculations performed by Möller [103] and Pashkevich [13] are in qualitative agreement with the data. They predicted that competition between symmetric and asymmetric fission is expected for nuclei around ^{227}Th. However, the only available quantitative prediction of Möller [103] on the transition from symmetry to asymmetry does not coincide with the data. In contrast to the data, this calculation predicted a transition along a line with approximately constant values of $N - Z$ of the fissioning system (see Figure 20).

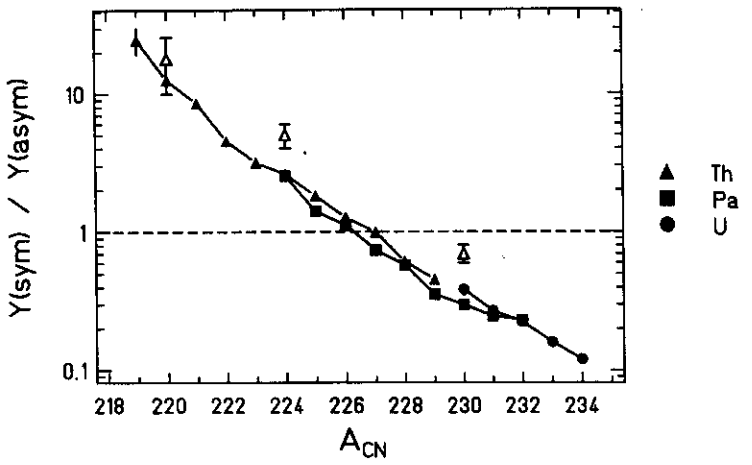

Figure 23: Intensity ratios of the symmetric and the asymmetric fission components in the transitional region as a function of mass number. The full triangles (squares, circles) correspond to thorium (protactinium, uranium) isotopes. The open symbols show data for ^{220}Th and ^{224}Th measured by Itkis et al. [32] and for ^{230}Th measured by Unik et al. [27].

The widths of the different components were determined from the data, too. As demonstrated in Figure 24, the widths of both the asymmetric and the symmetric component stay almost constant over the whole range of nuclei investigated. While the asymmetric component is supposed to be composed of two fission channels, standard I and standard II, the symmetric component may be identified with only one, the superlong channel. Therefore, we will con-

centrate on the symmetric component here. Since mass and nuclear charge of the fission fragments are highly correlated, the widths in charge and mass should approximately be related by the *A/Z* ratio of the fissioning system. Therefore, the present data may be compared to previous results deduced from mass distributions. For the large number of systems investigated in the present work, the width of the symmetric component varies only little. The width tends to decrease slightly with increasing neutron number of the system. The large fluctuations from system to system found in previous studies (see e.g. refs. [15,104]) are not present in the systems investigated here. We assume that the rather neutron-deficient systems studied in the present experiment give more reliable results for the characteristics of the symmetric fission channel than previous experiments on more neutron-rich isotopes, since the yield of the symmetric channel in low-energy fission decreases strongly with increasing mass number.

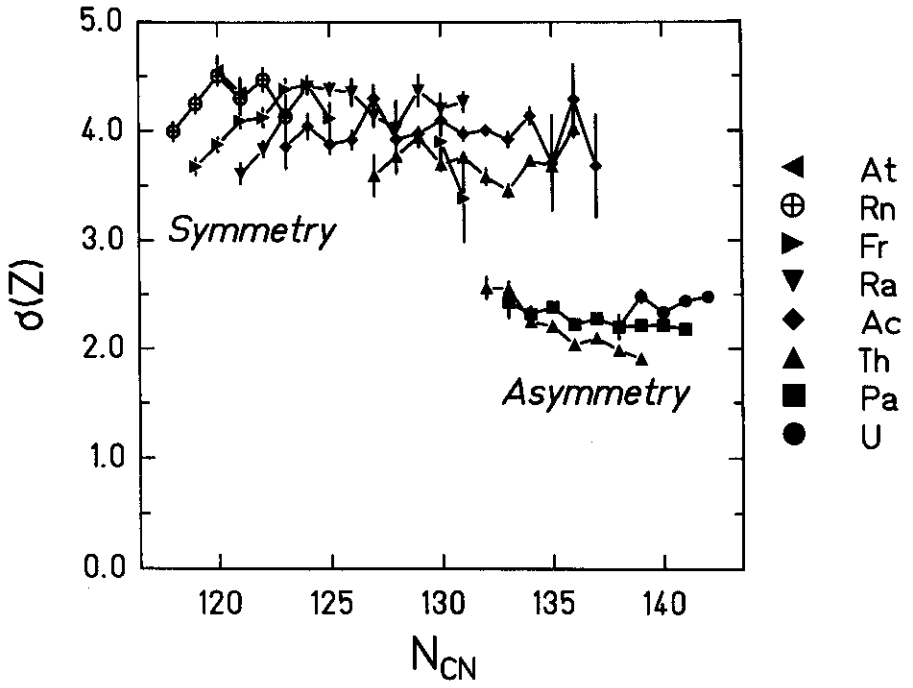

Figure 24: Widths (standard deviations) of the different components in the nuclear-charge distributions after electromagnetic-induced fission, measured in this experiment for different nuclei.

In detail, the charge-yield distributions and the total kinetic energies of ^{233}U, ^{228}Pa, ^{225}Th, ^{223}Th, ^{219}Ac, and ^{214}Ra for electromagnetic-induced fission are shown in Figure 25. A strong even-odd structure shows up for the uranium and thorium isotopes in both the asymmetric and the symmetric component. First, we will concentrate on the signatures of shell effects. In the nuclear-charge yields, the shell effects are responsible for the appearance of the asymmetric component. However, it may also cause a fine structure in the symmetric component as observed for nuclei near ^{201}Tl [105] or an abnormally narrow symmetric peak as observed for nuclei near ^{258}Fm [19]. The nuclear-charge distributions found in the present experiment for nuclei with $A < 220$ do not seem to show any clear signature of shell effects. They all have similar single-humped shapes. There might be an indication for a fine structure near symmetry in ^{214}Ra, similar to that found in ^{201}Tl, but the statistical significance is not very high.

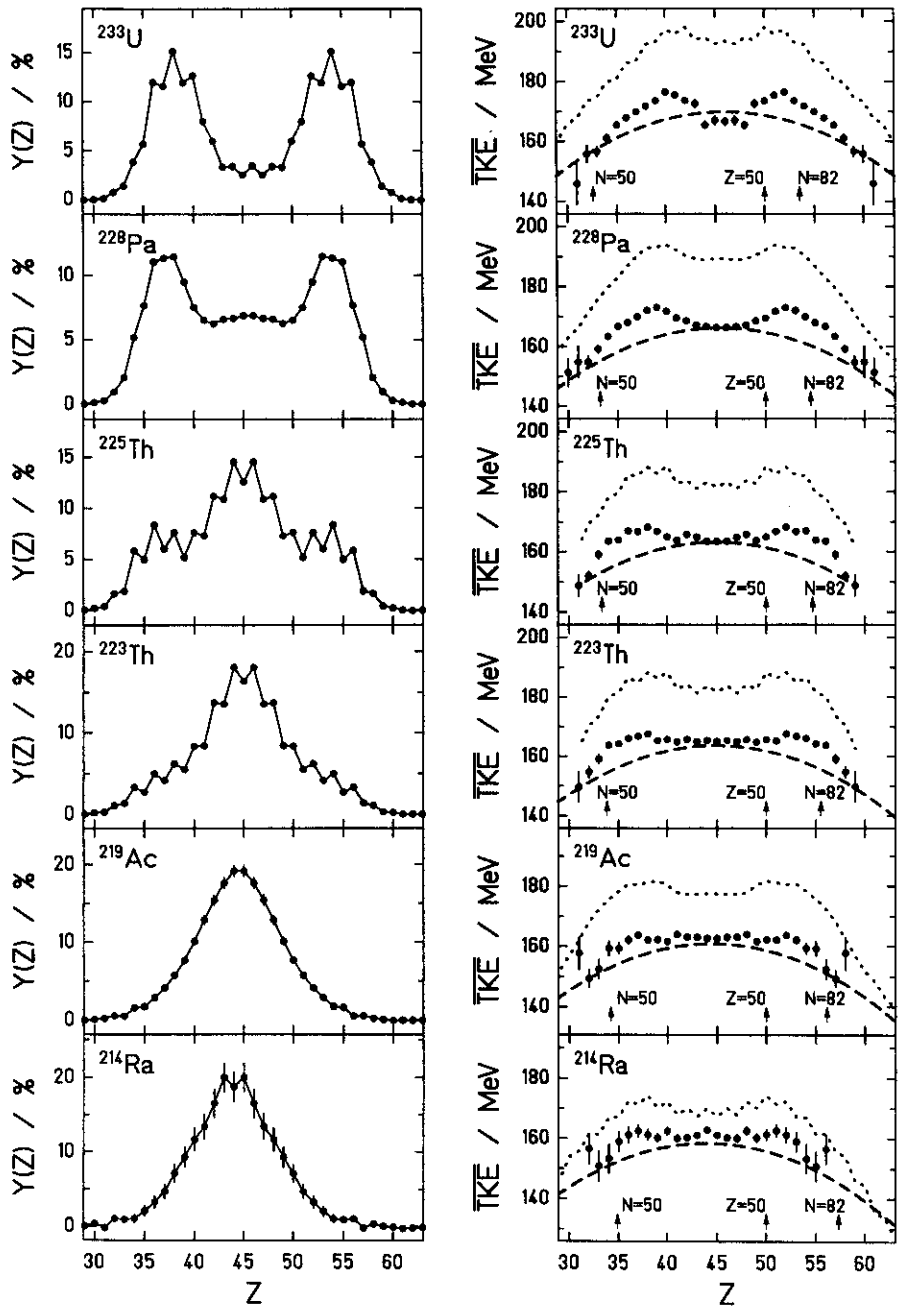

Figure 25: Elemental yields (left part) and average total kinetic energies (right part) as a function of the nuclear charge measured for fission fragments of several fissioning nuclei after electromagnetic excitations. Only statistical errors are given. The total kinetic energies are subject to an additional systematic uncertainty of 2 %, common to all data. In addition, for each charge split the maximum Q (ground-state to ground-state) value determined by varying the neutron numbers of the fission fragments is shown (dotted lines). Arrows indicate the positions of neutron (N = 50, 82) and proton shells (Z = 50). The positions of the neutron shells are calculated from the proton numbers by assuming an unchanged charge density (UCD). Finally, the expectations of a macroscopic scission-point model are shown (dashed lines) based on the Coulomb repulsion of the fragments at scission including a quadrupole deformation of $\beta_1 = \beta_2 = 0.625$ and a tip distance of d = 2 fm [11].

However, shell effects may also show up in the kinetic energies. Shell effects in the total kinetic energies become clearer, if the data are compared to a prediction on the basis of the liquid-drop model. For this purpose we used the following simplified description as proposed in the scission-point model of Wilkins et al. [11] without taking shell effects into account:

$$TKE = \frac{Z_1 \cdot Z_2 \cdot e^2}{D} \tag{11}$$

with

$$D = r_0 \cdot A_1^{1/3}\left(1+\tfrac{2}{3}\beta_1\right) + r_0 \cdot A_2^{1/3}\left(1+\tfrac{2}{3}\beta_2\right) + d \tag{12}$$

and r_0 = 1.16 fm. A_1, A_2, Z_1 and Z_2 are the mass and nuclear-charge numbers of the fission fragments. The other parameters are given in the caption of Figure 25.

The gross structural effects observed in the charge yields are different from those showing up in the total kinetic energies. From ^{233}U to ^{223}Th, the weight of the asymmetric fission component decreases, while the enhancement of the total kinetic energies (with respect to the expectation of the macroscopic model) for fission with a neutron number of the heavy fragment around N = 82 is preserved. For the lighter fissioning nuclei, the enhancement of the total kinetic energies moves away from N = 82 while the charge distributions become single humped. In all cases, the structure in the total kinetic energies as a function of the charge split is rather similar to the structure in the Q values. This means that the total excitation energy *TXE*, defined as *TXE* = Q - *TKE*, does not vary strongly as a function of charge split. However, the *TXE* values decrease systematically for the lighter systems, indicating that the scission configuration becomes more compact.

An interesting feature is that the structure in the total kinetic energy closely follows the magic numbers. For example, the position of the enhanced kinetic energy shifts according to the position of the N = 82 shell from ^{233}U to ^{233}Th. This behaviour strongly differs from that of the mean position of the nuclear charge yields of the asymmetric component that is strictly constant at Z = 54 as mentioned above. In addition, the enhanced total kinetic energies near magic neutron and proton numbers with respect to the macroscopic model show up with similar magnitudes for all nuclei, independently of their structure in the elemental yields. This is also true for those lighter nuclei that just show one symmetric fission component in the yields.

The corresponding element distributions and mean total kinetic energies after nuclear excitations, shown in Figure 26, are affected much less by nuclear-structure effects. Again only those fission events are considered which preserve the number of protons of the secondary projectiles. For the heavier nuclei, a small contribution of the asymmetric fission component is still clearly visible in the yields, but the distributions for the lighter nuclei at least qualitatively coincide with the expectation of the macroscopic model: The elemental yields are symmetric and Gaussian shaped, and the total kinetic energies agree rather well with the calculated Coulomb repulsion of the two nascent fragments in the scission configuration without considering any shell effects.

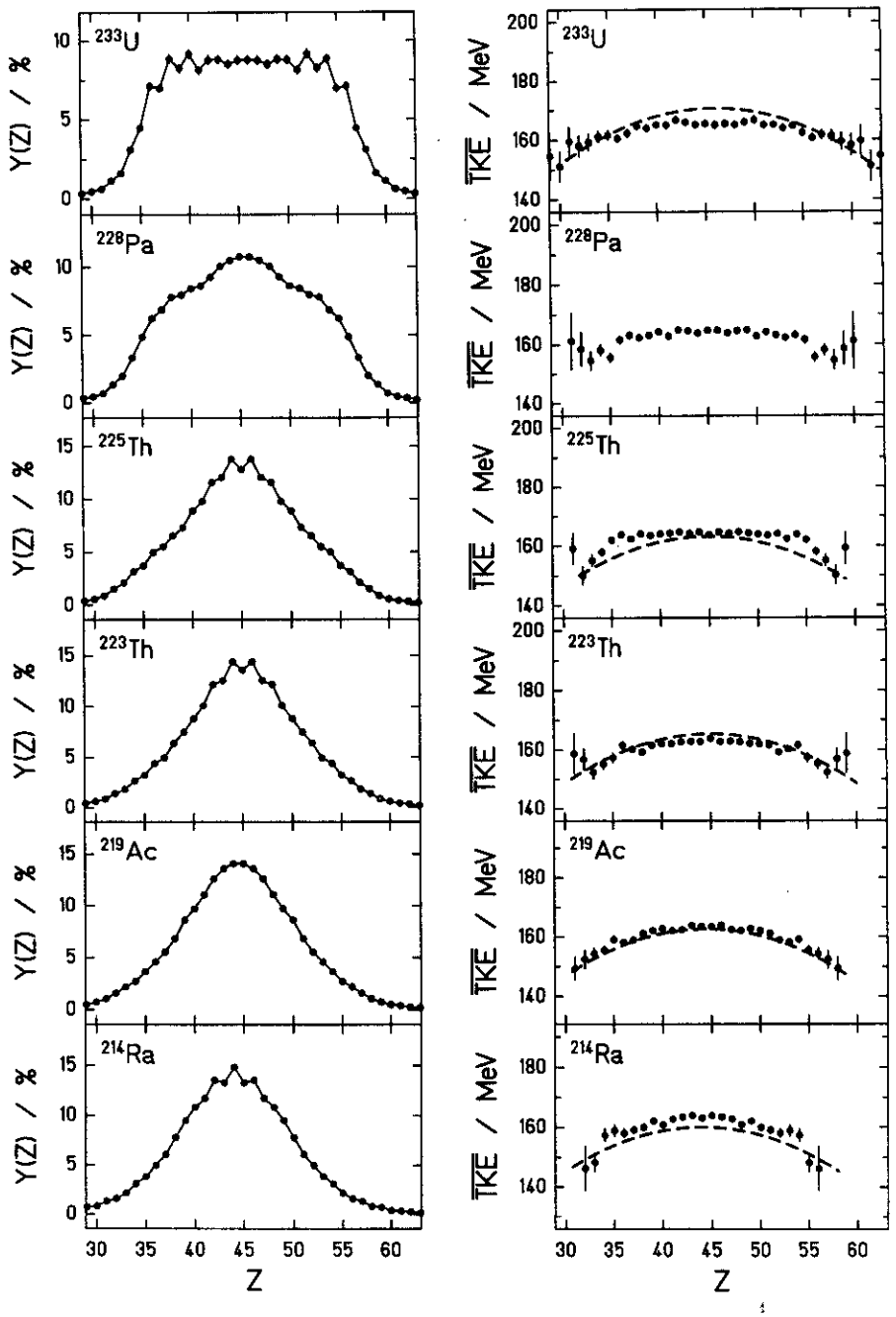

Figure 26: Elemental yields (left part) and average total kinetic energies (right part) as a function of the nuclear charge measured for fission fragments of several fissioning nuclei after nuclear excitations. Only statistical errors are given. The total kinetic energies are subject to an additional systematic uncertainty of 2%, common to all data. In addition, for each charge split the expectations of a macroscopic scission-point model are shown (dashed lines) based on the Coulomb repulsion of the fragments at scission including a quadrupole deformation of $\beta_1 = \beta_2 = 0.625$ and a tip distance of $d = 2$ fm [11].

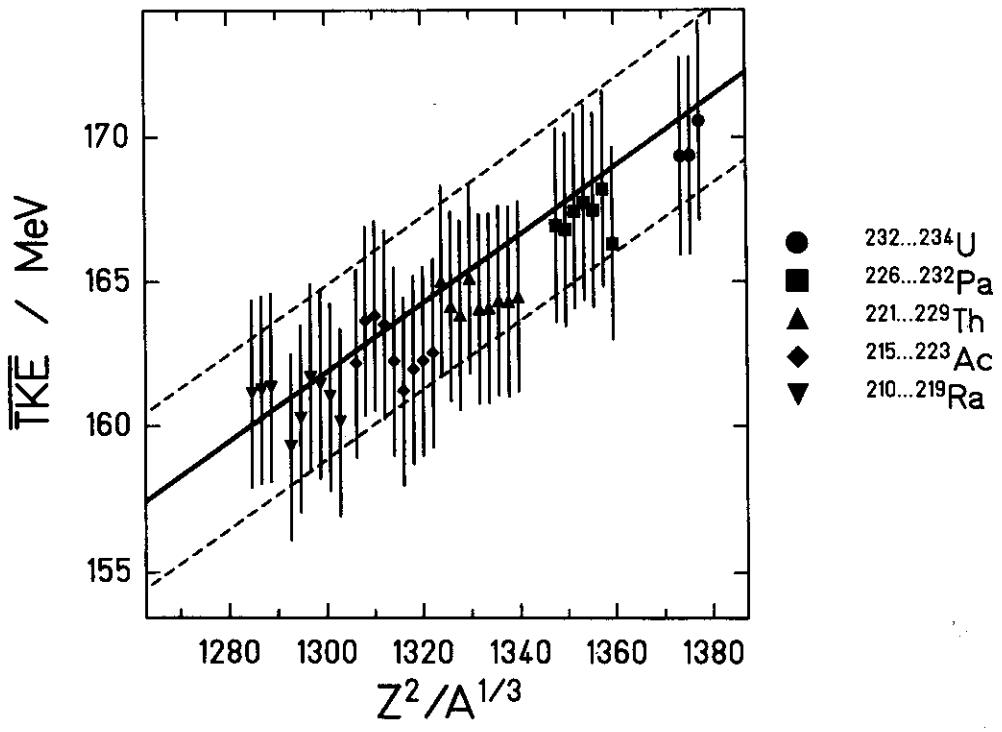

Figure 27: Comparison of the mean total kinetic energies measured in electromagnetic-induced fission, averaged over all charge splits, for all systems investigated (data points) with the systematics of Viola et al. [106] (full line). The error bars correspond to the systematical error of the experimental data of ±2%. The broken lines represent the uncertainty band of the systematics.

In Figure 27, the mean total kinetic energies, averaged over all charge splits, obtained in fission after electromagnetic excitation are compared with the systematics of Viola et al. [106] for all systems investigated. Both the absolute values and the tendency agree well with the systematics within the error bars.

A summary of the numerical results derived from the measured elemental yields and mean total kinetic energies after electromagnetic-induced fission is listed in Table 5. The beam time which was attributed to this experiment did not allow to cover all nuclei with the desirable amount of counting statistics. Therefore, the total kinetic energies are not given for all systems. Also the even-odd effects for radium and radon isotopes do not allow any detailed analysis, apart from the fact that the even-odd effect is in the order of 5 % to 8 %.

From the large number of systems investigated in the secondary-beam experiment described in this paper, new insight into pair breaking in fission has been acquired. Specific results have already been published [107]. We have shown that an appreciable even-odd effect in the elemental yields systematically shows up even in the fission of odd-Z elements where at least one unpaired proton is present. A similar observation has been made in two specific cases in thermal-neutron induced fission, ^{237}Np($2n_{th}$,f) [108] and ^{241}Am($2n_{th}$,f) [109,110]. From the present secondary-beam experiment it has become clear that even-odd structure in the fission yields of odd-Z fissioning nuclei is a general phenomenon. This finding is in con-

trast to the previous understanding as described in the introduction. According to the interpretation we give in ref.[107], part of the measured even-odd effect results from the different numbers of excited states available in the two nascent fragments. The unpaired protons are driven to the heavy fragment due to the higher phase space available. This finding implies that the relationship between the proton even-odd effect and pair-breaking processes in fission has to be reconsidered.

A more detailed discussion of the data acquired in the present work will be the subject of forthcoming publications. In particular the influence of nuclear composition and of excitation energy on the fission characteristics will be considered. We will discuss the implications of the systematic coverage of long isotopic chains obtained in the present experiment for an improved understanding of fission dynamics. In addition we will compare our data with results obtained recently at higher excitation energies, on multimodal fission of a few actinides near ^{227}Th [32,62].

The present experiment has also provided the fission cross sections of a large number of secondary projectiles after electromagnetic and nuclear excitations [66]. These results will be reported in a separate publication.

Table 5: Numerical results of the present work for the fission properties of all secondary projectiles investigated after electromagnetic excitation. The values given in the columns 2, 3, 4, and 5 result from a fit to the elemental yields with three Gaussian distributions. The numbers given in parentheses have been imposed to the fit. *TKE* values have been deduced only from measurements with high counting statistics. The global even-odd effect is listed only for even-*Z* fissioning nuclei since it is zero for odd-*Z* fissioning nuclei due to symmetry arguments.

Nucleus	Total width in *Z* (standard deviation)	Average *Z* of heavy asymmetric component	Width in *Z* of asymm. Component	width in *Z* of symm. Component	*Y*(sym)/ *Y*(asym)	Mean *TKE* / MeV	Global even-odd effect / %
^{234}U	7.83±0.02	53.79±0.05	2.48±0.04	(4.04)	0.12±0.01	171.9±3.4	12.5±1.1
^{233}U	7.82±0.01	53.91±0.03	2.44±0.02	(4.04)	0.16±0.01	172.0±3.4	10.9±0.6
^{232}U	7.72±0.02	53.99±0.04	2.33±0.03	(4.04)	0.22±0.01	173.2±3.5	9.9±0.9
^{231}U	7.67±0.04	53.99±0.08	2.48±0.06	(4.04)	0.27±0.02		10.1±1.5
^{230}U	7.51±0.08	54.11±0.14	2.20±0.11	(4.04)	0.39±0.03		8.2±2.8
^{232}Pa	8.09±0.02	54.03±0.04	2.18±0.03	(4.04)	0.23±0.01	169.5±3.4	
^{231}Pa	8.09±0.01	54.04±0.02	2.21±0.02	(4.04)	0.25±0.01	169.4±3.4	
^{230}Pa	8.03±0.01	54.10±0.03	2.21±0.02	(4.04)	0.30±0.01	170.0±3.4	
^{229}Pa	7.86±0.01	54.07±0.03	2.20±0.02	(4.04)	0.35±0.01	170.3±3.4	
^{228}Pa	7.40±0.01	53.97±0.02	2.28±0.02	(4.04)	0.58±0.01	170.1±3.4	
^{227}Pa	7.16±0.02	54.00±0.04	2.22±0.03	(4.04)	0.74±0.01	170.8±3.4	
^{226}Pa	6.66±0.02	53.87±0.05	2.38±0.04	(4.04)	1.11±0.02	168.9±3.4	
^{225}Pa	6.39±0.03	53.86±0.10	2.32±0.07	(4.04)	1.41±0.04		
^{224}Pa	5.81±0.05	53.94±0.20	2.43±0.14	(4.04)	2.52±0.13		
^{229}Th	8.09±0.03	54 10±0.05	1.91±0.04	(4.04)	0.45±0.01	167.6±3.4	19.7±1.2
^{228}Th	7.86±0.03	54.18±0.05	1.98±0.04	(4.04)	0.61±0.02	166.7±3.3	19.4±1.2
^{227}Th	7.23±0.04	54.08±0.07	2.10±0.05	(4.04)	1.00±0.03	166.4±3.3	13.9±1.2
^{226}Th	6.99±0.01	54.24±0.04	2.04±0.03	4.02±0.08	1.26±0.03	167.7±3.4	15.8±0.4
^{225}Th	6.30±0.01	54.01±0.06	2.21±0.04	3.68±0.06	1.82±0.04	166.7±3.3	14.0±0.4
^{224}Th	5.91±0.01	54.12±0.06	2.25±0.03	3.73±0.04	2.58±0.05	166.7±3.3	13.5±0.3

^{223}Th	5.33±0.01	53.58±0.13	2.55±0.06	3.45±0.06	3.14±0.12	167.0±3.3	11.8±0.4
^{222}Th	5.03±0.01	53.66±0.21	2.56±0.10	3.58±0.07	4.51±0.28	166.9±3.3	12.6±0.5
^{221}Th	4.74±0.02	(54)	(2.13)	3.76±0.04	8.5±0.3	167.1±3.3	9.3±0.6
^{220}Th	4.44±0.04	(54)	(2.13)	3.69±0.06	12.6±1.0		9.8±1.1
^{219}Th	4.44±0.05	(54)	(2.13)	3.94±0.09	24.9±5.3		5.1±1.5
^{218}Th	4.12±0.19	(54)	(2.13)	3.77±0.16	31.6±17.4		6.8±4.8
^{217}Th	4.47±0.17	(54)	(2.13)	3.59±0.19	30.4±16.7		7.8±4.0
^{226}Ac	5.73±0.17	53.34±0.42	1.89±0.32	3.68±0.47	2.4±0.5		
^{225}Ac	4.62±0.21	(54)	(2.13)	4.29±0.32	11.7±4.4		
^{224}Ac	3.76±0.41	(54)	(2.13)	3.70±0.43	9.2±3.6		
^{223}Ac	4.87±0.05	(54)	(2.13)	4.13±0.08	9.2±0.7	164.8±3.3	
^{222}Ac	4.48±0.04	(54)	(2.13)	3.92±0.03	11.8±0.9	166.2±3.3	
^{221}Ac	4.67±0.03	(54)	(2.13)	4.00±0.02	11.9±0.6	166.4±3.3	
^{220}Ac	4.40±0.04	(54)	(2.13)	3.97±0.03	16.5±1.4	166.1±3.3	
^{219}Ac	4.36±0.04	(54)	(2.13)	4.09±0.03	26.3±4.0	164.8±3.3	
^{218}Ac	4.53±0.04	(54)	(2.13)	3.97±0.03	15.4±1.3	163.8±3.3	
^{217}Ac	4.30±0.07	(54)	(2.13)	3.92±0.04	22.5±4.1	164.6±3.3	
^{216}Ac	4.28±0.07	(54)	(2.13)	4.29±0.06	>50	164.6±3.3	
^{215}Ac	4.10±0.07	(54)	(2.13)	3.92±0.04	49.2±18.5	164.9±3.3	
^{214}Ac	4.11±0.07	(54)	(2.13)	3.88±0.08	33.3±8.6		
^{213}Ac	4.22±0.08	(54)	(2.13)	4.04±0.11	48.2±22.5		
^{212}Ac	4.59±0.14	(54)	(2.13)	3.86±0.20	15.1±4.1		
^{219}Ra	4.00±0.12	(54)	(2.13)	4.26±0.09	34.6±13.4	163.7±3.3	0.3±2.5
^{218}Ra	4.31±0.11	(54)	(2.13)	4.20±0.14	33.4±13.9	163.9±3.3	0.8±2.4
^{217}Ra	4.44±0.09	(54)	(2.13)	4.37±0.14	47.9±25.6	163.9±3.3	3.1±2.3
^{216}Ra	3.92±0.23	(54)	(2.13)	4.02±0.25	27.2±15.6		2.5±5.0
^{215}Ra	4.11±0.12	(54)	(2.13)	4.14±0.10	28.3±7.8	161.9±3.2	0.7±2.8
^{214}Ra	4.68±0.08	(54)	(2.13)	4.35±0.12	27.2±7.5	162.9±3.3	0.1±2.0
^{213}Ra	4.30±0.06	(54)	(2.13)	4.38±0.06	>50	164.3±3.3	5.5±1.6
^{212}Ra	4.38±0.05	(54)	(2.13)	4.40±0.05	>50	164.0±3.3	1.7±1.4
^{211}Ra	4.32±0.06	(54)	(2.13)	4.15±0.09	>50	163.6±3.3	5.1±1.6
^{210}Ra	4.15±0.06	(54)	(2.13)	3.83±0.07	30.3±5.8	162.7±3.3	7.1±1.7
^{209}Ra	3.72±0.11	(54)	(2.13)	3.61±0.10	>50		6.1±2.7
^{218}Fr	3.89±0.40	(54)	(2.13)	3.38±0.40	>50		
^{217}Fr	3.77±0.28	(54)	(2.13)	3.90±0.18	>50		
^{212}Fr	4.29±0.13	(54)	(2.13)	4.12±0.14	>50		
^{211}Fr	4.32±0.09	(54)	(2.13)	4.42±0.08	>50		
^{210}Fr	4.53±0.07	(54)	(2.13)	4.38±0.10	>50		
^{209}Fr	4.33±0.07	(54)	(2.13)	4.12±0.09	>50		
^{208}Fr	4.25±0.06	(54)	(2.13)	4.09±0.07	>50		
^{207}Fr	4.11±0.06	(54)	(2.13)	3.88±0.07	>50		
^{206}Fr	3.93±0.07	(54)	(2.13)	3.68±0.08	>50		
^{209}Rn	4.22±0.16	(54)	(2.13)	4.13±0.16	44.7±1.7		2.3±3.6
^{208}Rn	4.80±0.08	(54)	(2.13)	4.47±0.11	34.2±0.7		4.0±1.9
^{207}Rn	4.36±0.11	(54)	(2.13)	4.30±0.14	>50		7.5±2.9
^{206}Rn	4.50±0.08	(54)	(2.13)	4.50±0.08	>50		5.2±2.1
^{205}Rn	4.15±0.10	(54)	(2.13)	4.25±0.09	>50		6.2±2.5
^{204}Rn	3.94±0.10	(54)	(2.13)	4.00±0.09	>50		13.8±2.6
^{206}At	4.27±0.16	(54)	(2.13)	4.34±0.14	>50		
^{205}At	4.61±0.11	(54)	(2.13)	4.55±0.14	>50		

7. CONCLUSION

The present work reports on a recent application of secondary beams for nuclear-fission studies in inverse kinematics. The experiment had to combine several stages. First, the nuclei of interest had to be produced, separated and identified. Secondly, excited states in the vicinity of the fission barrier were populated by electromagnetic excitations in a secondary lead target. Finally, the fission fragments were registered, and their elemental yields as well as their total kinetic energies were determined. In view of the low secondary-beam intensity of about 100 particles of a specific isotope per second, the success of the experiment essentially depended on the application of a very efficient excitation mechanism and on the high detection efficiency of the experimental set up. The high beam energy plays a key role in the present experiment. In contrast to most secondary-beam experiments of the first generation that are designed to determine a specific property of the secondary projectiles like binding energy or total interaction cross section, the present experiment is a quite elaborate secondary-reaction study where complex characteristics of the fission process could be investigated.

The most important achievements of the secondary-beam experiment are the rather free choice of the nucleus to be investigated, independent of its chemical properties and independent of its radioactive decay characteristics, down to half-lives in the order of 100 ns, the excellent nuclear-charge resolution for all fission fragments, and the remarkably good determination of the mean total kinetic energies with uncertainties in the order of 10^{-5} of the laboratory energies. In particular, the large number of high-quality nuclear-charge distributions reveals the important progress attained by the new experimental technique.

In the present experiment, the low-energy fission properties of 70 short-lived nuclear species have been studied, almost all of them for the first time. In particular, the transition from symmetric to asymmetric fission around ^{227}Th has been covered systematically. The mass of the fissioning nucleus showed up as the appropriate scaling parameter that determines the weight of the two fission components. In asymmetric fission, the average nuclear charge of the heavy fission fragment was observed to be fixed at $Z = 54$. The total kinetic energies showed particularly high values for fragments with neutron numbers close to $N = 82$ in the heavy fragment. Large even-odd effects, even for symmetric charge splits, were found.

The huge amount of new data acquired in the present experiment could not exhaustively be discussed in the present publication. The data contain much more information relevant for the understanding of the fission process than could be touched here. However, the present paper was primarily intended to describe the novel experimental technique in full detail. We gave a general overview on the potential progress in nuclear fission brought about by the new data. More elaborate discussions on special topics have been published already or will be the subject of forthcoming publications.

ACKNOWLEDGEMENT

We are indebted to K.-H. Behr, A. Brünle and K. Burkhard and their team for the technical support of the experiment. H. Folger and his colleagues of the target laboratory provided the targets, stripper foils and degrader layers. The experiment would not have been possible without the efforts of the accelerator crew to provide a constant ^{238}U beam with the required intensity. Critical remarks of P. Armbruster to the manuscript are gratefully acknowledged.

This work has been supported by the GSI Hochschulprogramm and by the Bundesministerium für Bildung, Wissenschaft, Forschung und Technologie under contract number BMBF 06 DA 473. The responsibility rests with the authors.

REFERENCES

[1] K.-H. Schmidt, A. Heinz, H.-G. Clerc, B. Blank, T. Brohm, S. Czajkowski, C. Donzaud, H. Geissel, E. Hanelt, H. Inrich, M. C. Itkis, M. de Jong, A. R. Junghans, A. Magel, G. Münzenberg, F. Nickel, M. Pfützner, A. Piechaczek, C. Röhl, C. Scheidenberger, W. Schwab, S. Steinhäuser, K. Sümmerer, W. Trinder, B. Voss, S. V. Zhdanov, Phys. Lett. **B 325** (1994) 313.

[2] T. Aumann, K. Sümmerer, H. Geissel, B. Blank, T. Brohm, H.-G. Clerc, S. Czajkowski, C. Donzaud, A. Grewe, E. Hanelt, A. Heinz, H. Irnich, M. de Jong, A. R. Junghans, J. V. Kratz, A. Magel, G. Münzenberg, F. Nickel, M. Pfützner, A. Piechaczek, C. Röhl, C. Scheidenberger, K.-H. Schmidt, W. Schwab, S. Steinhäuser, W. Trinder, B. Voss, Z. Phys. **A 352** (1995) 163.

[3] P. Armbruster, M. Bernas, S. Czajkowski, H. Geissel, T. Aumann, Ph. Dessagne, C. Donzaud, E. Hanelt, A. Heinz, M. Hesse, C. Kozhuharov, Ch. Miehe, G. Münzenberg, M. Pfützner, K.-H. Schmidt, W. Schwab, C. Stéphan, K. Sümmerer, L. Tassan-Got, B. Voss, Z. Phys. **A 355** (1996) 191.

[4] C. Donzaud, S. Czajkowski, P. Armbruster, M. Bernas, C. Böckstiegel, Ph. Dessagne, H. Geissel, E. Hanelt, A. Heinz, C. Kozhuharov, Ch. Miehe, G. Münzenberg, M. Pfützner, W. Schwab, C. Stéphan, K. Sümmerer, L. Tassan-Got, B. Voss, Eur. Phys. J. **A 1** (1998) 407.

[5] W. Schwab, M. Bernas, P. Armbruster, S. Czajkowski, Ph. Dessagne, C. Donzaud, H. Geissel, A. Heinz, C. Kozhuharov, C. Miehe, G. Münzenberg, M. Pfützner, C. Stéphan, K. Sümmerer, L. Tassan-Got, B. Voss, Eur. Phys. J. **A 2** (1998) 179.

[6] Th. Rubehn, W. F. J. Müller, R. Bassini, M. Begemann-Blaich, Th. Blaich, A. Ferrero, C. Gross, G. Imme, I. Iori, G. J. Kunde, W. D. Kunze, V. Lindenstruth, U. Lynen, T. Möhlenkamp, L. G. Moretto, B. Ocker, J. Pochodzalla, G. Raciti, S. Reito, H. Sann, A. Schüttauf, W. Seidel, V. Serfling, W. Trautmann, A. Trizcinski, G. Verde, A. Wörner, E. Zude, B. Zwieglinski, Z. Phys. **A 353** (1995) 197.

[7] Th. Rubehn, R. Bassini, M. Begemann-Blaich, Th. Blaich, A. Ferrero, C. Gross, G. Imme, I. Iori, G. J. Kunde, W. D. Kunze, V. Lindenstruth, U. Lynen, T. Möhlenkamp, L. G. Moretto, W. F. J. Müller, B. Ocker, J. Pochodzalla, G. Raciti, S. Reito, H. Sann, A. Schüttauf, W. Seidel, V. Serfling, W. Trautmann, A. Trzcinski, G. Verde, A. Wörner, E. Zude, B. Zwieglinski, Phys. Rev. **C 53** (1996) 3143.

[8] M. Göppert-Mayer, Phys. Rev. **74** (1948) 235.

[9] L. Meitner, Nature **165** (1950) 561.

[10] P. Fong, Phys. Rev. **102** (1956) 434.

[11] B. D. Wilkins, E. P. Steinberg, R. R. Chasman, Phys. Rev. **C 14** (1976) 1832.

[12] A. Turkevich, J. B. Niday, Phys. Rev. **84** (1951) 52.

[13] V. V. Pashkevich, Nucl. Phys. **A 169** (1971) 275.

[14] M. G. Mustafa, U. Mosel, H. W. Schmitt, Phys. Rev. **C 7** (1973) 1519.

[15] U. Brosa, S. Grossmann, A. Müller, Phys. Rep. **197** (1990) 167.

[16] K. F. Flynn, E. P. Horwitz, C. A. A. Bloomquist, R. F. Barnes, R. K. Sjoblom, P. R. Fields, L. E. Glendenin, Phys. Rev. **C 5** (1972) 1725.
[17] D. C. Hoffman, J. B. Wilhelmy, J. Weber, W. R. Daniels, E. K. Hulet, R. W. Lougheed, J. H. Landrum, J. F. Wild, R. J. Dupzyk, Phys. Rev. **C 21** (1980) 972.
[18] E. K. Hulet, J. F. Wild, R. J. Dougan, R. W. Lougheed, J. H. Landrum, A. D. Dougan, M. Schädel, R. L. Hahn, P. A. Baisden, C. M. Henderson, R. J. Dupyzk, K. Sümmerer, G. Behune, Phys. Rev. Lett. **56** (1986) 313.
[19] E. K. Hulet, J. F. Wild, R. J. Dougan, R. W. Lougheed, J. H. Landrum, A. D. Dougan, P. A. Baisden, C. M. Henderson, R. J. Dupzyk, R. L. Hahn, M. Schädel, K. Sümmerer, G. Bethune, Phys. Rev. **C 40** (1989) 770.
[20] D. C. Hoffman, M. R. Lane, Radiochimica Acta **70/71** (1995) 135.
[21] H. Faissner, K. Wildermuth, Phys. Lett. **2** (1962) 212.
[22] P. Möller, J. R. Nix, Proc. Symp. on Phys. and Chem. of Fission, Rochester 1973, **vol 1**, (Vienna, IAEA, 1974), pp 329.
[23] V. V. Pashkevich, Nucl. Phys. **A 477** (1988) 1.
[24] S. Cwiok, P. Rozmej, A. Sobiczewski, Z. Patyk, Nucl. Phys. **A 491** (1989) 281.
[25] R. C. Jensen, A. W. Fairhall, Phys. Rev. **109** (1958) 942.
[26] H. C. Britt, H. E. Wegner, J. C. Gursky, Phys. Rev. **129** (1963) 2239.
[27] J. P. Unik, J. R. Huizenga, Phys. Rev. **134B** (1964) 90.
[28] E. Konecny, H. W. Schmitt, Phys. Rev. **172** (1968) 1213.
[29] H. J. Specht, Rev. Mod. Phys. **46** (1974) 773.
[30] H. J. Specht, Phys. Scripta **10A** (1974) 21.
[31] J. Weber, H. C. Britt, A. Gavron, E. Konecny, J. B. Wilhelmy, Phys. Rev. **C 13** (1976) 2413.
[32] M. G. Itkis, Yu. Ts. Oganessian, G. Chubarian, V. N. Okolovich, G. N. Smirenkin, in Nuclear Fission and Fission-product Spectroscopy, H. Faust and G. Fioni (eds.), ILL Grenoble (1994), pp. 77.
[33] M. Itkis, V. N. Okolovich, A. Ya, Rusanov, G. N. Smirenkin, Yad. Fiz. 41 (1985) 849 (Sov. J. Nucl. Phys. **41** (1985) 544).
[34] R. W. Hasse, Nucl. Phys. **A 128** (1969) 609.
[35] J. R. Nix, Nucl. Phys. **A 130** (1969) 241.
[36] P. Möller, S. G. Nilsson, Phys. Lett. **31 B** (1970) 283.
[37] H. Kudo, H. Muramatsu, H. Nakahara, K. Miyano, I. Kohno, Phys. Rev. **C 25** (1982) 3011.
[38] M. G. Itkis, V. N. Okolovich, A Ya, Rusanov, G. N. Smirenkin, Particles and Nuclei, JINR, Dubna, Moscow, Atomizdat. **19** (1988) 701 (Sov. J. Part. Nucl. **19** (1988) 301).
[39] G. A. Kudyaev, Yu. B. Ostapenko, G. N. Smirenkin, Yad. Fiz. **45** (1987) 1534 (Sov. J. Nucl. Phys. **45** (1987) 951).
[40] G. A. Kudyaev, Yu. B. Ostapenko, E. M. Rastopchin, Yad. Fiz. **47** (1988) 1540 (Sov. J. Nucl. Phys. **47** (1988) 976).
[41] W. Nörenberg, Z. Phys. **197** (1966) 246.
[42] J. W. Negele, S. E. Koonin, P. Möller, J. R. Nix, A. J. Sierk, Phys. Rev. **C 17** (1978) 1098.
[43] J. F. Berger, M. Girod, D. Gogny, Nucl. Phys. A **428** (1984) 23c.
[44] F. A. Ivanyuk, H. Hofmann, V. V. Pashkevich, S. Yamaji, Phys. Rev. **C 55** (1997) 1730.

[45] H. Hofmann, D. Kiderlen, Phys. Rev. **C 56** (1997) 1025.
[46] S. Amiel, H. Feldstein, Phys. Rev. **C 11** (1975) 845.
[47] H. Nifenecker, G. Mariolopoulos, J. P. Bocquet, R. Brissot, Mme Ch. Hamelin, J. Crancon, Ch. Ristori, Z. Phys. **A 308** (1982) 39.
[48] F. Gönnenwein, "Mass, Charge and Kinetic Energy of Fission Fragments" in "The Nuclear Fission Process", CRC Press, London, 1991, C. Wagemans, ed., pp 409.
[49] E. Moll, H. Schrader, G. Siegert, M. Ashgar, J. P. Bocquet, C. Bailleul, J. P. Gautheron, J. Greif, G. I. Crawford, C. Chauvin, H. Ewald, H. Wollnik, P. Armbruster, G. Fiebig, H. Lawin, K. Sistemich, Nucl. Instr. Meth. **123** (1975) 615.
[50] H.-G. Clerc, K.-H. Schmidt, H. Wohlfarth, W. Lang, H. Schrader, K. E. Pferdekämper, R. Jungmann, M. Ashgar, J. P. Bocquet, G. Siegert, Nucl. Phys. **A 247** (1975) 74.
[51] G. Siegert, J. Greif, H. Wollnik, G. Fiedler, R. Decker, M. Ashgar, G. Bailleul, J. P. Bocquet, J. P. Gautheron, H. Schrader, P. Armbruster, H. Ewald, Phys. Rev. Lett. **34** (1975) 1034.
[52] W. Lang, H.-G. Clerc, H. Wohlfarth, H. Schrader, K.-H. Schmidt, Nucl. Phys. **A 345** (1980) 34.
[53] C. Schmitt, A. Guessous, J. P. Bocquet, H.-G. Clerc, R. Brissot, D. Engelhardt, H. R. Faust, F. Gönnenwein, M. Mutterer, H. Nifenecker, J. Pannicke, Ch. Ristori, J. P. Theobald, Nucl. Phys. **A 430** (1984) 21.
[54] U. Quade, K. Rudolph. S. Skorka, P. Armbruster, H.-G. Clerc, W. Lang, M. Mutterer, C. Schmitt, J. P. Theobald, F. Gönnenwein, J. Pannicke, H. Schrader, G. Siegert, D. Engelhardt, Nucl. Phys. **A 487** (1988) 1.
[55] J. P. Bocquet, R. Brissot, H. R. Faust, M. Fowler, J. Wilhelmy, M. Ashgar, M. Djebara, Z. Phys. **A 335** (1990) 41.
[56] A. Oed, P. Geltenbort, R. Brissot, F. Gönnenwein, P. Perrin, E. Aker, D. Engelhardt, Nucl. Instr. Meth. **219** (1984) 569.
[57] P. Koczon, M. Mutterer, J. P. Theobald, P. Geltenbort, F. Gönnenwein, A. Oed, M. S. Moore, Phys. Lett. **B 191** (1987) 249.
[58] F. Gönnenwein, Radiation Effects **94** (1986) 205.
[59] J. L. Sida, P. Armbruster, M. Bernas, J. P. Bocquet, R. Brissot, H. R. Faust, Nucl. Phys. **A 502** (1989) 233c.
[60] R. Hentschel, H. R. Faust, H. O. Denschlag, B. D. Wilkins, J. Gindler, Nucl. Phys. **A 571** (1994) 427.
[61] S. A. Kreek, H. L. Hall, K. E. Gregorich, R. A. Henderson, J. D. Leyba, K. R. Czerwinski, B. Kadkodayan, M. P. Neu, C. D. Kacher, T. M. Hamilton, M. R. Lane, E. R. Sylwester, A. Tuerler, D. M. Lee, M. J. Nurmia, D. C. Hoffman, Phys. Rev. **C 50** (1994) 2288.
[62] I. Nishinaka, Y. Nagame, K. Tsukada, H. Ikezoe, K. Sueki, H. Nakahara, M. Tanikawa, T. Ohtsuki, Phys. Rev. **C 56** (1997) 891.
[63] H.-G. Clerc, M. de Jong, T. Brohm, M. Dornik, A. Grewe, E. Hanelt, A. Heinz, A. R. Junghans, C. Röhl, S. Steinhäuser, B. Voss, C. Ziegler, K.-H. Schmidt, S. Czajkowski, H. Geissel, H. Irnich, A. Magel, G. Münzenberg, F. Nickel, A. Piechacyek, C. Scheidenberger, W. Schwab, K. Sümmerer, W. Trinder, M. Pfützner, B. Blank, A. Ignatyuk, G. Kudyaev, Nucl. Phys. **A 590** (1995) 785.
[64] A. R. Junghans, M. de Jong, H.-G. Clerc, A. V. Ignatyuk, G. A. Kudyaev, K.-H. Schmidt, Nucl. Phys. **A 629** (1998) 635.

[65] C. Böckstiegel, S. Steinhäuser, J. Benlliure, H.-G. Clerc, A. Grewe, A. Heinz, M. de Jong, A. R. Junghans, J. Müller, K.-H. Schmidt , Phys. Lett. **B 398** (1997) 259.

[66] A. Heinz, PhD thesis, IKDA, TU Darmstadt, 1998.

[67] H. Geissel, P. Armbruster, K.-H. Behr, A. Brünle, K. Burkard, M. Chen, H. Folger, B. Franczak, H. Keller, O. Klepper, B. Langenbeck, F. Nickel, F. Pfeng, M. Pfützner, E. Roeckl, K. Rykaczewski, I. Schall, D. Schardt, C. Scheidenberger, K.-H. Schmidt, A. Schröter, T. Schwab, K. Sümmerer, M. Weber, G. Münzenberg, T. Brohm, H.-G. Clerc, M. Fauerbach, J.-J. Gaimard, A. Grewe, E. Hanelt, B. Knödler, M. Steiner, B. Voşs, J. Weckenmann, C. Ziegler, A. Magel, H. Wollnik, J.P. Dufour, Y. Fujita, D. J. Vieira, B. Sherrill, Nucl, Instr. Meth. **B 70** (1992) 286.

[68] K.-H. Schmidt, E. Hanelt, H. Geissel, G. Münzenberg, J.-P. Dufour, Nucl. Instr. Meth. **A 260** (1987) 287.

[69] B. Voss, T. Brohm, H.-G. Clerc, A. Grewe, E. Hanelt, A. Heinz, M. de Jong, A. Junghans, W. Morawek, C. Röhl, S. Steinhäuser, C. Ziegler, K.-H. Schmidt, K.-H. Behr, H. Geissel, G. Münzenberg, F. Nickel, C. Scheidenberger, K. Sümmerer, A. Magel, M. Pfützner, Nucl. Instr. Meth. **A 364** (1995) 150.

[70] M. de Jong, K.-H. Schmidt, B. Blank, C. Böckstiegel, T. Brohm, H.-G. Clerc, S. Czajkowski, M. Dornik, H. Geissel, A. Grewe, E. Hanelt, A. Heinz, H. Irnich, A. R. Junghans, A. Magel, G. Münzenberg, F. Nickel, M. Pfützner, A. Piechaczek, C. Scheidenberger, W. Schwab, S. Steinhäuser, K. Sümmerer, W. Trinder, B. Voss, C. Ziegler, Nucl. Phys. **A 628** (1998) 479.

[71] A. R. Junghans, PhD thesis, IKDA, TU Darmstadt, 1998.

[72] C. J. Benesh, B. C. Cook, J. P. Vary, Phys. Rev. **C 40** (1989) 1198.

[73] A. Grewe, S. Andriamonje, C. Böckstiegel, T. Brohm, H.-G. Clerc, S. Czajkowski, E. Hanelt, A. Heinz, M. G. Itkis, M. de Jong, A. Junghans, M. S. Pravikoff, K.-H. Schmidt, W. Schwab, S. Steinhäuser, K. Sümmerer, B. Voss, Nucl. Phys. **A 614** (1997) 400.

[74] J.R. Cummings, W.R. Binns, T.L. Garrard, M.H. Israel, J. Klarmann, E.C. Stone, C.J. Waddington, Phys. Rev. **C 42** (1990) 2530.

[75] G. Baur, C. A. Bertulani, Phys. Rev. **C 34** (1986) 1654.

[76] P. F. Bortignon, A. Bracco, R. A. Broglia, Giant Resonances, Nuclear Structure at Finite Temperature, New York: Harwood Acad. (1998).

[77] J. Speth, ed., Intern. Rev. Nucl. Phys. **7** (1991) (Spec. issue).

[78] W. J. Llope, P. Braun-Munzinger, Phys. Rev. **C 41** (1990) 2644.

[79] W. J. Llope, P. Braun-Munzinger, Phys. Rev. **C 45** (1992) 799.

[80] T. Aumann, C. A. Bertulani, K. Sümmerer, Phys. Rev. **C 51** (1995) 416.

[81] K. Boretzky, J. Stroth, E. Wajda, T. Aumann, Th. Blaich, J. Cub, Th. W. Elze, H. Emling, W. Henning, R. Holzmann, H. Klingler, R. Kulessa, J. V. Kratz, D. Lambrecht, Y. Leifels, E. Lubkiewicz, K. Stelzer, W. Walus, M. Zinser, E. Zude, Phys. Lett. **B 384** (1996) 30.

[82] E. K. Warburton, J. Weneser, in: "Isospin in Nuclear Physics", ed. D. H. Wilkinson (Wiley, New York, NY, USA, 1969), p. 173.

[83] J. Speth, A. v. d. Woude, Rep. Prog. Phys. **44** (1981) 719.

[84] R. Pitthan, Proc. Nucl. Sci. Res. Conf. on Giant Multipole Resonances, Oak Ridge 1979, ed. F. E. Bertrand (Harwood Academic Publishers, Chur 1980), p. 161.

[85] L. J. Lindgren, A. S. Soldatov, Yu. M. Tsipenyuk, Yad. Fiz. 32 (1980) 335 (Sov. J. Nucl. Phys. **32** (1980) 173).

[86] B. L. Berman, J. T. Caldwell, E. J. Dowdy, S. S. Dietrich, P. Meyer, R. A. Alvarez, Phys. Rev. **C 34** (1986) 2201.
[87] J.-J. Gaimard, K.-H. Schmidt, Nucl. Phys. **A 531** (1991) 709.
[88] A. V. Ignatyuk, G. A. Kudyaev, A. Junghans, M. de Jong, H.-G. Clerc, K.-H. Schmidt, Nucl. Phys. **A 593** (1995) 519.
[89] M. Asghar, F. Caitucolli, B. Leroux, P. Perrin, G. Barreau, Nucl. Phys. **A 368** (1981) 328.
[90] J. Kaufmann, W. Mollenkopf, F. Gönnenwein, P. Geltenbort, A. Oed, Z. Phys. **A 341** (1992) 319.
[91] S. Pommé, E. Jacobs, K. Persyn, D. De Frenne, K. Govaert, M. L. Yoneama, Nucl. Phys. **A 560** (1993) 689.
[92] K. Persyn, E. Jacobs, S. Pommé, D. de Frenne, K. Govaert, M. L. Yoneama, Nucl. Phys. **A 620** (1997) 171.
[93] F. Farget, A. V. Ignatyuk, A. R. Junghans, K.-H. Schmidt, submitted to Nucl. Phys. **A**
[94] M. Dahlinger, D. Vermeulen, K.-H. Schmidt, Nucl. Phys. **A 376** (1982) 94.
[95] G. Audi, O. Bersillon, J. Blachot, A. H. Wapstra, Nucl. Phys. **A 624** (1997) 1.
[96] V. M. Kupriyanov, G. N. Smirenkin, B. I. Fursov, Yad. Fiz. 39 (1984) 281 (Sov. J. Nucl. Phys. **39** (1984) 281).
[97] A. I. Sergachev, N. P. D'Yachenko, A. M. Kovalev, B. D. Kuz'minov, Yad. Fiz. 16 (1972) 475 (Sov. J. Nucl. Phys. **16** (1973) 266).
[98] S. Nagy, K. E. Flynn, J. E. Gindler, J. W. Meadows, L. E. Glendenin, Phys. Rev. **C 17** (1978) 163.
[99] L. E. Glendenin, J. E. Gindler, J. Ahmad, D. J. Henderson, J. W. Meadows, Phys. Rev. **C 22** (1980) 152.
[100] L. E. Glendenin, J. E. Gindler, D. J. Henderson, J. W. Meadows, Phys. Rev. **C 24** (1981) 2600.
[101] J. E. Gindler, L. E. Glendenin, D. J. Henderson, J. W. Meadows, Phys. Rev. **C 27** (1983) 2058.
[102] I. F. Croall, J. G. Cuninghame, Nucl. Phys. **A 125** (1969) 402.
[103] P. Möller, Nucl. Phys. **A 192** (1972) 529.
[104] L. Dematte, C. Wagemans, R. Barthelemy, P. D'hondt, A. Deruytter, Nucl. Phys. **A 617** (1997) 331.
[105] S. I. Mulgin, K.-H. Schmidt, A. Grewe, S. V. Zhdanov, Nucl. Phys. **A 640** (1998) 375.
[106] V. E. Viola, K. Kwiatkowski, M. Walker, Phys. Rev. **C 31** (1985) 1550.
[107] S. Steinhäuser, J. Benlliure, C. Böckstiegel, H.-G. Clerc, A. Heinz, A. Grewe, M. de Jong, A. R. Junghans, J. Müller, M. Pfützner, K.-H. Schmidt, Nucl. Phys. **A 634** (1998) 89.
[108] M. Davi, J. O. Denschlag, I. Tsekhanovitch, M. Wöstheinrich, H. Faust, S. Oberstedt, Gerade-Ungerade-Effekte in der Spaltreaktion ^{237}Np($2n_{th}$,f), DPG-Tagung "Hadronen und Kerne" (Göttingen 1997).
[109] P. Siegler, T. Schunk, M. Mutterer, W. Schwab, J. P. Theobald, U. Quade, H. Faust, Proc. Internat. Workshop on Dyn. Aspects of Nucl. Fission, Smolenice Castle 1991, J. Kristiak and B. I. Pustylnik eds., JINR Dubna, 1992, p. 260.
[110] P. Stumpf, H. O. Denschlag, H. R. Faust, Proc. Seminar on Fission, ed. C. Wagemans (Pont D'Oye, Belgium, 1995) p. 196.